



Provided by the author(s) and University of Galway in accordance with publisher policies. Please cite the published version when available.

Title	Damaged beyond repair? Characterising the damage zone of a fault late in its interseismic cycle, the Alpine Fault, New Zealand
Author(s)	Williams, Jack N.; Toy, Virginia G.; Massiot, Cécile; McNamara, David D.; Wang, Ting
Publication Date	2016-07-25
Publication Information	Williams, Jack N., Toy, Virginia G., Massiot, Cécile, McNamara, David D., & Wang, Ting. (2016). Damaged beyond repair? Characterising the damage zone of a fault late in its interseismic cycle, the Alpine Fault, New Zealand. <i>Journal of Structural Geology</i> , 90, 76-94. doi: http://dx.doi.org/10.1016/j.jsg.2016.07.006
Publisher	Elsevier
Link to publisher's version	https://doi.org/10.1016/j.jsg.2016.07.006
Item record	http://hdl.handle.net/10379/6729
DOI	http://dx.doi.org/10.1016/j.jsg.2016.07.006

Downloaded 2024-04-25T07:34:48Z

Some rights reserved. For more information, please see the item record link above.



1 **Damaged beyond repair? Characterising the damage zone of a fault late in its**
2 **interseismic cycle, the Alpine Fault, New Zealand**

3

4 Jack N. Williams^{a*}, Virginia G. Toy^a, Cécile Massiot^b, David D. McNamara^c, Ting
5 Wang^d

6 **Affiliations:**

7 *^aDepartment of Geology, University of Otago, PO Box 56, Dunedin 9054, New*
8 *Zealand*

9 *^bSchool of Geography, Environment, and Earth Sciences, Victoria University of*
10 *Wellington, PO Box 600, Wellington 6012, New Zealand*

11 *^cGNS Science, PO Box 30-368, Lower Hutt 5040, New Zealand*

12 *^dDepartment of Mathematics and Statistics, University of Otago, PO Box 56, Dunedin*
13 *9054, New Zealand*

14 **Email addresses:**

15 Jack Williams: jack.williams@otago.ac.nz

16 Virginia G. Toy: virginia.toy@otago.ac.nz

17 Cécile Massiot: Cecile.Massiot@vuw.ac.nz

18 David D. McNamara: D.McNamara@gns.cri.nz

19 Ting Wang: ting.wang@otago.ac.nz

20 ***Corresponding Author:** Jack Williams^a (email: jack.williams@otago.ac.nz, Ph:
21 +64 275271455)

22 **Keywords:** damage zone, Alpine Fault, fault-healing, DFDP, fracture density

23 **Abstract**

24 X-ray computed tomography (CT) scans of drill-core, recovered from the first phase
25 of the Deep Fault Drilling Project (DFDP-1) through New Zealand's Alpine Fault,
26 provide an excellent opportunity to study the damage zone of a plate-bounding
27 continental scale fault, late in its interseismic cycle. Documentation of the
28 intermediate-macro scale damage zone structures observed in the CT images show
29 that there is no increase in the density of these structures towards the fault's principal
30 slip zones (PSZs), at least within the interval sampled, which is 30 m above and
31 below the PSZs. This is in agreement with independent analysis using borehole
32 televiewer data. Instead, we conclude the density of damage zone structures to
33 correspond to lithology. We find that 72% of fractures are fully healed, by a
34 combination of clays, calcite and quartz, with an additional 24% partially healed. This
35 fracture healing is consistent with the Alpine Fault's late interseismic state, and the
36 fact that the interval of damage zone sampled coincides with an alteration zone, an
37 interval of extensive fluid-rock interaction. These fractures do not impose a reduction
38 of P-wave velocity, as measured by wireline methods. Outside the alteration zone
39 there is indirect evidence of less extensive fracture healing.

40

41 **1. Introduction**

42 Fault zone structure analysis concerns the three dimensional manifestations of a fault,
43 such as its thickness, geometry, and continuity of slip surfaces (Chester and Logan,
44 1986; Faulkner et al., 2008; Wibberley et al., 2008). These features are classically

45 described with reference to a 'fault core' and 'damage zone' (Caine et al., 1996).
46 Under this terminology, the fault core accommodated the majority of brittle strain and
47 generally consists of cataclasites and gouges. The surrounding damage zone is
48 typically a zone of enhanced fracturing, subsidiary faulting, and other deformation
49 related features (Anders and Wiltschko, 1994; Vermilye and Scholz, 1998; Schulz and
50 Evans, 2000; Wilson et al., 2003; Mitchell and Faulkner, 2009; Johri et al., 2014;
51 Jeppson and Tobin, 2015). The damage zone is significantly wider than the fault core
52 and may host single (Figure 1a) or multiple anastomosing fault cores (Figure 1b)
53 (Faulkner et al., 2008).

54

55 Fault zones are the product of the subtle interplay between and within different
56 components of their system such as their structure, mechanical properties, and
57 composition (Faulkner et al., 2010). Thus, though damage zones accommodate only a
58 small amount of displacement relative to the fault core, they are strongly coupled with
59 many other fault zone properties. In particular, there exist feedback relationships
60 between the damage zone and the stress state around the fault (Faulkner et al., 2006),
61 its permeability (Wibberley and Shimamoto, 2003; Lockner et al., 2009; Mitchell and
62 Faulkner, 2012), elastic properties (Griffith et al., 2009; Gudmundsson et al., 2010),
63 and the dynamics of earthquake rupture (Andrews, 2005; Rice et al., 2005; Weng et
64 al., 2016).

65

66 However, the exact nature of these relationships is liable to change with time since
67 damage zones evolve through the seismic cycle. In this cycle, fractures are opened by
68 coseismic faulting and then progressively healed during the interseismic period by

69 closing or precipitation of secondary minerals (Sibson, 1990; Chester et al., 1993; Li
70 and Vidale, 2001; Tenthorey and Cox, 2006; Lin et al., 2007; Wästeby et al., 2014).
71 By using the example of New Zealand's Alpine Fault, we are able to report on a fault
72 that is understood to be late in its interseismic cycle (Berryman et al., 2012; Townend
73 et al., 2013), and so can investigate how fault healing since the last major Alpine
74 Fault rupture has influenced its damage zone.

75

76 The Alpine Fault is also an attractive target for damage zone characterisation as off-
77 fault processes are occurring within a rock mass that contains lithological variations
78 (Toy et al., 2015). This allows for assessment of how lithology competes with other
79 influences on damage zone formation, such as distance from the fault core (Chester et
80 al., 2005; Savage and Brodsky, 2011; Johri et al., 2014), the displacement the fault
81 has accommodated (Beach et al., 1999; Fossen and Hesthammer, 2000; Faulkner et
82 al., 2011; Savage and Brodsky, 2011) and variations in confining pressure (Ben-Zion
83 and Shi, 2005; Lund Snee et al., 2014; Ishii, 2015), fault geometry (Chester and
84 Chester, 2000; Childs et al., 2009; Finzi et al., 2009; Bistacchi et al., 2010; Lin and
85 Yamashita, 2013) and frictional properties (Savage and Cooke, 2010).

86

87 Here we examine a record of the Alpine Fault's damage zone provided by X-ray
88 computed tomography scans of drill core from the first phase of the Alpine Fault,
89 Deep Fault Drilling Project (DFDP-1, <http://alpine.icdp-online.org>). Results are then
90 combined with lithological characterisation of the drill-core (Toy et al., 2015) and
91 wireline logs of the DFDP-1 boreholes (Townend et al., 2013) to: (1) provide an
92 assessment of the spatial distribution of damage zone structures around the DFDP-1

93 boreholes, (2) offer direct evidence of how, for a fault late in its interseismic cycle,
94 the damage zone has healed, and (3) explore what effect this healing has on the elastic
95 properties of the surrounding rock mass.

96

97 **2. Geological setting of the Alpine Fault**

98 *2.1 Tectonic setting*

99 The Alpine Fault is a major transpressive structure that extends for 850 km (~660 km
100 onshore) along the west side of the South Island of New Zealand. Here it is the main
101 structure forming the boundary between the Pacific and Australian plates (Figure 2a),
102 accommodating slip at ~70% of the rates indicated by the NUVEL-1A interplate
103 velocity vectors (DeMets et al., 1994; Norris and Cooper, 2001). This study focuses
104 on the central section of the Alpine Fault between Hokitika and Haast (Figure 2b),
105 which has been the focus of DFDP, a multiphase scientific drilling programme that
106 aims to directly sample the structure and ambient conditions of the Alpine Fault at
107 depth (Townend et al., 2009).

108

109 Paleoseismic, geodetic and seismological observations indicate that the Alpine Fault
110 is locked above depths of 12-18 km (Wallace et al., 2007) and that it fails in large
111 ($M_w > 7$) and possibly great ($M_w > 8$) earthquakes (Sutherland et al., 2007; De Pascale
112 and Langridge, 2012). A stratigraphic record of past earthquakes, spanning 8000
113 years on the southern section of the Alpine Fault, indicate that the fault has a
114 recurrence interval of 329 ± 68 years (Berryman et al., 2012). Since the last
115 large/great earthquake occurred in 1717 AD (Wells et al., 1999; De Pascale and

116 Langridge, 2012) the Alpine Fault is statistically in the late phase of its interseismic
117 cycle. This makes it a globally significant site for the study of tectonic deformation
118 (Townend et al., 2009), particularly in the case of fault damage zones that evolve over
119 the seismic cycle (Chester et al., 1993; Lin et al., 2007; Wästeby et al., 2014).

120

121 *2.2 Alpine Fault zone structure*

122 At the regional scale, the central section of the Alpine Fault is approximately a
123 moderately southeast dipping, dextral-reverse, planar fault. It separates basement,
124 granitic, and gneissic Australian plate rocks in the footwall - that in places are
125 overlain by Quaternary gravels - from Pacific plate, amphibolite facies (oligoclase-
126 zone) quartzofeldspathic Alpine Schist in the hanging wall (Norris and Cooper, 2007).
127 Adjacent to the principal slip zones (PSZs) of the fault in the hanging wall (Figure
128 2c), the schist grades into protomylonites, mylonites, and ultramylonites (Reed, 1964;
129 Sibson et al., 1981; Cooper and Norris, 1994; Norris and Cooper, 1997, 2007; Toy,
130 2008). These units are considered to be accommodating motion along the Alpine
131 Fault by a combination of dislocation creep and grain-size-sensitive creep in a 1-2 km
132 thick shear zone below the seismogenic portion of the Alpine Fault (Norris and
133 Cooper, 2007; Toy et al., 2015). Immediately overlaying the PSZs is an interval of
134 cataclasite derived from the adjacent mylonites (Figure 2c). This is interpreted to have
135 been generated through brittle deformation and pressure solution-accommodated
136 grain-size sensitive creep, occurring towards the base of the seismogenic zone (Warr
137 and Cox, 2001; Toy et al., 2015).

138

139 This same sequence was also encountered in the first phase of DFDP drilling (DFDP-
140 1) that took place at the extensively studied Alpine Fault exposure at Gaunt Creek
141 (Sutherland et al., (2012); Toy et al., (2015), Figure 2b). This site saw the completion
142 of two vertical boreholes: DFDP-1A to a depth of ~100 m and DFDP-1B to a depth of
143 ~152 m. Interpretations from the wireline suites in DFDP-1A and DFDP-1B
144 (Townend et al., 2013) were integrated with drill-core descriptions to provide a
145 classification scheme for the DFDP-1 lithologies (Toy et al., 2015).

146

147 The structurally reworked rocks that Toy et al. (2015) described are compatible with
148 the Caine et al. (1996) conceptual fault zone model. The fault core consists of the
149 cataclasites and gouges (units 3-6 of Toy et al., 2015) that demonstrably
150 accommodated the majority of brittle displacement along the Alpine Fault.

151 Surrounding these units are heavily fractured ultramylonites and breccias (units 1, 2
152 and 7 of Toy et al., 2015) that constitute the damage zone.

153

154 Defining the boundary between the fault core and damage zone for the DFDP-1 drill-
155 core is problematic. Firstly the rocks that span the damage zone-fault core transition
156 are overprinted by a pervasive “alteration zone.” This is broadly defined by
157 Sutherland et al. (2012) as a zone of enhanced fluid-rock interaction within which
158 there has been extensive carbonate and phyllosilicate neomineralisation.

159

160 Secondly, in the depth interval of ~69-80 m in DFDP-1A, and ~96-116 m in DFDP-
161 1B, damage zone mylonites and fault core cataclasites are interlayered (Toy et al.,
162 2015). It is only below these depth intervals that the DFDP-1 drill-core consistently

163 comprises cataclasites (units 3-6), and it is these depths that we define as the
164 boundary between the fault core and damage zone (i.e. 80 m in DFDP-1A, 116 m in
165 DFDP-1B).

166

167 Finally, strain within the fault core has been further localised to <0.5 m thick gouges
168 that comprise the PSZs and were interpreted to define active or recently abandoned
169 slip surfaces. These were intercepted at measured depths (MD) of 90.75 m in DFDP-
170 1A and 128.20 and 143.85 m in DFDP-1B. The gouges have a distinct set of
171 geophysical properties: low resistivity, density, and P wave velocity, and high
172 spontaneous potential (Townend et al., 2013). They have a finer grain size and
173 distinct mineralogy (particularly the presence of smectite) compared to the
174 surrounding cataclasites (Boulton et al., 2014). Furthermore they have comparably
175 low permeability (10^{-20} m²) (Boulton et al., 2012) and under fluid-saturated
176 conditions, low frictional strength (Ikari et al., 2014). These properties set up the
177 conditions necessary for dynamic hydrologic processes, such as thermal
178 pressurisation (Sibson, 1973; Lachenbruch, 1980), that facilitates localisation of co-
179 seismic slip at shallow depths onto the PSZs (Carpenter et al., 2014; Ikari et al., 2014;
180 Mitchell and Toy, 2014). Therefore, herein we consider the spatial distribution of
181 damage around the boreholes with regards to proximity to the fault core and to the
182 PSZs.

183

184 **3. Methods**

185 *3.1 X-ray Computed Tomography*

186 A qualitative and quantitative analysis of the Alpine Fault damage zone was
187 performed using X-ray Computed Tomography (CT) scan images of the DFDP-1
188 drill-core. Drill-core was retrieved from ~31% and ~36% of the DFDP-1A and
189 DFDP-1B boreholes respectively (Toy et al., 2015). Drill-core recovery was focused
190 around the PSZs and so a near continuous record of rocks extending distances of <35
191 m from the PSZs exists. Since an alteration zone extends <50 m from the PSZs in the
192 DFDP-1 boreholes (Sutherland et al., 2012), the drill-core analysed in this study lies
193 substantially within this zone.

194

195 CT scanning provides a quick, non-destructive means to three-dimensionally image
196 objects based on the extent to which they attenuate X-rays passing through them.
197 Attenuation is a function of the material's atomic number (Z) and density; though the
198 extent to which either one of these properties attenuates X-rays is also a factor of the
199 X-ray energy (Ketcham and Carlson, 2001).

200

201 During CT scanning, the raw intensity data of the detected X-rays are converted
202 linearly to a CT number, which in this study corresponds to the 12-bit Hounsfield
203 Unit (HU) scale. Two-dimensional, transverse image slices of the object are
204 constructed with the CT numbers represented by a greyscale. Under the HU scale, air
205 is assigned a CT number of -1000 and is black, whereas materials with anomalously
206 high density or Z values, such as calcite, are assigned higher CT numbers and appear

207 white. Further information about CT scanning and its application to geosciences is
208 outlined by Ketcham and Carlson (2001).

209

210 A total of 23.2 m of drill-core from DFDP-1A and 50.5 m from DFDP-1B, that
211 covered all lithological units described by Toy et al., 2015, except unit 7 breccias, was
212 scanned at the Oncology Department of Dunedin Hospital. The Phillips Accolade
213 scanner was operated at 200 mA, with a Beam Quality of 8.4 mm, and a Half Value
214 Layer of 120 kVp. The horizontal slice spacing was 1 mm, field of view was 50 mm,
215 and the image size was 1024 x 1024 pixels. This results in a voxel size of 0.244 x
216 0.244 x 1 mm in the x, y and z directions respectively. Reconstruction of two-
217 dimensional CT slices into three-dimensional images of the drill-core was performed
218 using OsiriX Imaging Software (<http://www.osirix-viewer.com/>).

219

220 *3.2 Classification of damage zone structures in CT images*

221 We documented all damage zone structures observed in the CT images. We note that
222 damage zones do not necessarily include just fractures, but host a continuum of
223 features that form as the fault accommodates displacement, such as subsidiary faults,
224 and a gradual change (i.e. a rotation) of foliation orientation (Schulz and Evans, 1998;
225 Faulkner et al., 2010; Savage and Brodsky, 2011). Therefore, we use the umbrella
226 term ‘damage zone structure’ to define any feature recognised in the CT images that
227 constitutes the Alpine Fault damage zone (Table 1).

228

229 In the CT images, damage zone structures are represented by an aligned group of
230 voxels or pixels with anomalous CT numbers relative to the surrounding matrix

231 (Wennberg et al., 2009), and with a distinct edge so that it is possible to differentiate
232 them from the mylonitic foliation also apparent in the CT images (Figure 3a). Given
233 the dimensions of a voxel in the acquired CT data, only structures with an aperture >1
234 mm (i.e. larger than one pixel in the z direction) are considered. Thus this study is
235 primarily concerned with intermediate to macroscale damage around the Alpine Fault.

236

237 Damage zone structures were manually picked and categorised into different types
238 based on their aperture, the CT number of their fill and its texture (Table 1). The
239 colours used to label the different structures relate to the greyscale that was used to
240 visualise the CT scan images (with a CT number window of 500-4000). In the
241 damage zone structure classification used in this study (Table 1), the filling of gouge
242 and cataclasite in type i and ii structures respectively, indicates that they have
243 accommodated some localised strain and so represent subsidiary faults.

244

245 Lithological units 3, 4 and 6 of Toy et al., (2015) are defined by the presence of
246 cataclasite implying that they have been previously extensively fractured (Sibson,
247 1977; Chester and Chester, 1998) during accommodation of delocalised shear strain
248 in the fault core. We note, however, that the cataclasite fabric has been cross cut by a
249 later generation of damage zone structures, and it is these structures that we account
250 for in this study (Figure 3b and c).

251

252 Damage zone structures (type iii - viii) represent different types of fractures (Table 1).
253 By correlation to visual core logs, dark grey and grey fractures (type iii and iv) are
254 observed to be clay filled fractures. The low CT numbers (<0) in type v fractures

255 indicate densities similar to air and so represent open fractures, whilst fractures that
256 contain a range of low and moderate CT numbers (type vi and vii) signify partially
257 open fractures. Quartz and calcite veins are represented by white fractures (type viii).
258 Other features associated with fault damage zones, such as rotation of foliation or
259 mineralogical changes (Schulz and Evans, 1998, 2000) were not recognised in the CT
260 images.

261

262 *3.3 Differentiation of natural and induced fractures in DFDP-1 drill-core*

263 In distinguishing damage zone structures in drill-core, we need to take account of, and
264 remove fractures that may have been induced during drilling, coring or handling
265 processes. Fractures reported as handling-induced were identified from visual core
266 logs and removed from this analysis (Figure 3a). To identify fractures induced by
267 drilling or coring we apply the frameworks developed by Kulander et al., (1990) and
268 Keren and Kirkpatrick, (2016). Kulander et al., (1990) proposes that all fractures with
269 a fill are natural. Therefore only black/open fractures (type v, Table 1) may represent
270 induced fractures. Drill-core was washed immediately after recovery (Sutherland et
271 al., 2011), so that the chance of any induced fractures being filled with drilling mud
272 was minimal. Nevertheless, we cannot be certain that drilling mud was removed from
273 all induced fractures.

274

275 Of the induced fractures types described by Kulander et al., (1990), some form with a
276 distinct morphology. In this way, we identified disc fractures that tend to be sub-
277 horizontal and contain convex tops and concave bottoms (Figure 3d), and that form in
278 response to a vertical tension imposed by removal of the overlaying drilled rock

279 column (Kulander et al., 1990; Keren and Kirkpatrick, 2016). In foliated rocks, disc
280 fractures may be inclined with respect to the foliation (Kulander et al., 1990).

281 Therefore, where we see black/open (type v) fractures parallel to the foliation in the
282 mylonites, we also consider these to be induced structures (Figure 3a).

283

284 Some intervals of DFDP-1 drill-core show significant brecciation (Figure 3e and f).

285 The presence of slickenslides on individual clasts is typically used to determine if this
286 is natural or induced (Keren and Kirkpatrick, 2016). Unfortunately DFDP-1 drill-core
287 has been sub-sampled to the extent that it is not possible to make these observations.

288 However, we consider that natural brecciation in DFDP-1 drill-core typically results
289 in the development of a cataclasite fabric with rounded clasts, (Figure 3f), since they
290 have been sheared (Storti et al., 2007; Bjørk et al., 2009). Some intervals of breccia
291 within the mylonite units show evidence of *in situ* fragmentation with angular clasts
292 (Figure 3e). These breccias are interpreted to have been induced by drilling.

293

294 There are also some open fractures that occur in triangular sets and in which the apex
295 of the triangle points towards the centre of the core (Figure 3g). These are interpreted
296 as per Keren and Kirkpatrick, (2016) to be induced fractures, formed due to vertical
297 flexure of the core. Finally, open fractures with mineralised surfaces were not omitted
298 from this analysis, since they represent natural permeable fractures or fractures that
299 opened during core recovery. Despite the careful approach described above, we
300 cannot categorically rule out that some induced fractures were not removed from this
301 analysis; also some induced fractures may have exploited pre-existing fractures.

302

303 *3.4 Quantitative analysis of the density and distribution of damage zone structures*

304 To measure how damage zone structures are distributed around the Alpine Fault, we
305 measured the intersection depth of any structure along a 1D core-axial scan line
306 within a 2D CT image slice of DFDP-1 drill-core (Figure 4). The DFDP-1 boreholes
307 are vertical and so this scan line represents a vertical line. We then applied a weighted
308 moving average to this dataset, to illustrate the distribution and density of damage
309 zone structures. Our justification for using this statistical measure is twofold as
310 explained in the following.

311

312 *3.4.1 Accurate representation of the distribution of damage zone structures*

313 Previous studies of fault damage zones sampled by boreholes typically represent the
314 distribution of damage zone structures by binning them into depth intervals (e.g
315 Barton and Zoback, 1992; Yeh et al., 2007; Johri et al., 2014). The frequency of
316 fractures within each depth bin is then represented in a histogram. However, these
317 histograms are based on disjoint bins, and thus may fail to capture intervals of
318 anomalously high or low structure density that exist across the boundary of two
319 consecutive bins. For example, for the hypothetical fracture dataset shown in Figure
320 5a there is an interval of high fracture density at ~10 m depth. If fractures are binned
321 into 5 m intervals (Figure 5b), the 10 m depth acts as a boundary between two bins
322 thus splitting high fracture density across two bins (i.e. the bins at 5-10 m and 10-15
323 m) and obscuring its observation. This can be partially addressed by reducing the bin
324 size (Figure 5c). However, this will increase the amount of noise in the data resulting
325 in a “jagged histogram” (Wand, 1997).

326

327 In this study, we performed a moving average calculation to determine the
328 distribution of damage zone structures. In this calculation, the density is calculated
329 within a window of a predetermined depth interval centred on each depth. For
330 example for depth i , and a moving window size $2x+1$, the moving average (MA) is
331 calculated as:

$$MA(i) = \frac{1}{2x + 1} \sum_{i-x}^{i+x} n_{damage\ zone\ structures}$$

332 (1)

333 In this way, a continuous measurement of density is made, which more adequately
334 captures variations in the depth distribution of the damage zone structures. When
335 applied to the fracture dataset in Figure 5a, the region of high fracture density at ~10
336 m depth is well represented (Figure 5d). Caution must be applied when selecting the
337 size of the moving window to ensure an appropriate size is used, otherwise this
338 method can excessively smooth the data. Furthermore, if there was a boundary across
339 which there was an abrupt change in the density of damage zone structures, this may
340 be more effectively represented by a discrete binning method with an appropriate bin
341 size.

342

343 *3.4.2 Correction for orientation sampling bias*

344 The density of structures derived from the number of their intersections along a 1D
345 scan line should account for an orientation bias in which structures (sub) parallel to
346 the scan line are under-sampled (Terzaghi, 1965; Barton and Zoback, 1992; Priest,
347 1993). In order to account for this, each damage zone structure was assigned a
348 statistical weight, w , (Terzaghi, 1965):

$$w = \frac{1}{\cos\delta}$$

349 (2)

350 where δ is the acute angle between the normal plane to a structure and the scan line,
 351 with a maximum value of $w=10$, which corresponds to an angle of $\delta = 84.3^\circ$, to limit
 352 the overestimation of w (Priest, 1993; Massiot et al., 2015). Since the scan line
 353 represents a vertical line, δ is equivalent to the true dip of the damage zone structure.
 354 DFDP-1 drill-core is not oriented (Sutherland et al., 2011) and so the orientation of
 355 structures was measured within a local drill-core reference frame applying the
 356 convention described in Figure 4. A weighted moving average (*WMA*) was then
 357 calculated in which the density of damage zone structures for a given depth (i) is
 358 calculated from the sum of w of all damage zone structures found within a moving
 359 window $2x+1$, divided by the length of the window as expressed by:

$$WMA(i) = \frac{1}{2x + 1} \sum_{i-x}^{i+x} w_{\text{damage zone structures}}$$

360 (3)

361 This correction for orientation bias was also applied to the hypothetical dataset in
 362 Figure 5a to illustrate its effect on the calculation of fracture density. The corrected
 363 fracture population was represented by both binning into depth intervals (represented
 364 by weighted histograms, where the frequency of each bin is the sum of ' w ' of all
 365 fractures within each bin, Figure 5b and c), and by using a weighted moving average
 366 (Figure 5d). In both cases a higher fracture density is calculated at intervals where
 367 steeply dipping fractures intersect the vertical scan line. This more accurately reflects
 368 the density of steeply dipping fractures that are not accounted for in the uncorrected
 369 calculations.

370

371 However, the weighting does add a bias, since it is only applied to the intervals where
372 a steeply dipping fracture has been sampled. This implies that all the unsampled
373 steeply dipping fractures, which are required for the correction, are located at the
374 same depths as where they were sampled in the borehole. This could consequently
375 overestimate the fracture density for these depths. In short, applying a weighted
376 moving average will provide information on the density of poorly oriented fractures
377 within a rock mass, but not their distribution across the rock mass. For this reason, we
378 show results for cases where the Terzaghi weighting correction has, and has not been
379 applied to damage zone structure distribution in the DFDP-1 boreholes. To fully
380 account for density and distribution of fractures in a rock mass, ideally two mutually
381 perpendicular scan lines or a circular scan line should be employed (Mauldon et al.,
382 2001; Watkins et al., 2015).

383

384 For this study a weighted moving average was calculated at intervals of 2 cm depth. A
385 moving window of 1 m was used unless otherwise stated. Where there was
386 incomplete drill-core recovery, the size of the moving window was reduced by the
387 length of the interval of missing drill-core.

388

389 We also apply the weighted and non-weighted moving averages techniques to the
390 documented density of damage zone structures picked in the acoustic borehole
391 televiewer (BHTV) logs of the DFDP-1B borehole (McNamara, 2015). BHTV data
392 are continuously recorded with depth and the acquired image has a consistent quality
393 throughout (Townend et al., 2013), removing the need to normalise for missing

394 intervals or zones of variable quality. However, a BHTV log has a lower resolution
395 than CT images; it reveals structures only with an aperture of >5 mm and with a
396 significant acoustic contrast with the rock hosting the structure (Figure 6). Thus a
397 moving window of 5 m was used and the density of damage zone structures was
398 calculated at 10 cm intervals.

399

400 **4. Results**

401 *4.1 Density and distribution of damage zone structures*

402 The densities of damage zone structures, which are apparent from CT images of
403 DFDP-1A and 1B drill-core, are shown in Figure 7 and Figure 8 respectively. The CT
404 images show no increase in the density of damage zone structures towards either the
405 fault core or the PSZs. Indeed the core sections with the highest density of structures
406 are those at depths of 39-45 m from DFDP-1B, which have the greatest distance (<89
407 m) from PSZ-1 sampled in DFDP-1.

408

409 Initial interpretations of BHTV data for the DFDP-1B borehole indicate no increase in
410 the density of damage zone structures towards either the fault core or the PSZ
411 (Townend et al., 2013). A revision of these data (McNamara, 2015), which is
412 included in Figure 8, does indicate a small degree of non-monotonic increasing
413 damage immediately above PSZ-1 (105-125 m), regardless of whether a correction
414 for orientation bias is added. The overall lower density of damage zone structures in
415 the BHTV dataset compared to the drill-core CT images reflects its lower resolution
416 as described above. The damage zone structures most consistently sampled by the

417 BHTV are type i, ii and type v structures (Table 1), which tend to be the structures
418 with the highest aperture.

419

420 Though we note no, or very little, control on damage zone structure density with
421 proximity to the PSZs, it is apparent that some noticeable trends in the damage zone
422 structure density profiles coincide with lithological changes (Figure 7 and Figure 8).
423 For example at ~100, 106 and 116 m in DFDP-1B, a drop in the density of damage
424 zone structures corresponds to a transition from unit 3 cataclasites to unit 2
425 ultramylonites. This is qualitatively observed in the CT images (Figure 9). Damage
426 zone structure density is low below PSZ-1 in DFDP-1B (128.2 m depth) within the
427 footwall cataclasites, and below 81 m in DFDP-1A in an interval dominated by
428 hanging-wall foliated cataclasites.

429

430 The profile for the corrected density of damage zone structures (calculated using a
431 weighted moving average) tends to follow the uncorrected profile (calculated using a
432 moving average, Figure 7 and Figure 8). This suggests that the distribution of steeply
433 dipping damage zone structures, that are poorly oriented for intersection by the
434 DFDP-1 boreholes, is fairly homogenous. The interval 43-45 m in DFDP-1B is an
435 exception to this. This reflects the fact that it has a particularly high density of steeply
436 dipping structures, which is not accounted for in the uncorrected profile.

437

438 *4.2 Effect of damage zone structures on the elastic properties of the rock mass*

439 Of the damage zone structures observed in the CT images of DFDP-1 drill-core that
440 are located within the alteration zone of the Alpine Fault (that is all DFDP-1A drill-

441 core and all DFDP-1B drill-core at depths >94 m), 96% of fractures were healed to
442 some extent (i.e. only 4% exhibited no evidence of filling, and so were classed as
443 open type v structures) and 72% were fully healed (i.e. only 28% were open or
444 partially open, type v-vii structures, Table 1).

445

446 In order to constrain the influence of damage zone structures on the elastic properties
447 of the rock mass surrounding the Alpine Fault, we compare the density of damage
448 zone structures in the DFDP-1 boreholes to the P-wave velocity (V_P) of the boreholes.
449 These were obtained by wireline logging and previously presented in Townend et al.
450 (2013). Previous studies have shown that the presence of damage zone fractures may
451 reduce V_P around a fault at a range of scales (e.g. Stierman and Kovach, 1979;
452 Jeppson et al., 2010; Jeanne et al., 2012; Rempe et al., 2013; Jeppson and Tobin,
453 2015). Qualitative comparisons of V_P logs to damage zone structure density (Figure 7
454 and Figure 8) show that intervals of high damage zone structure density (e.g. 125-127
455 m, DFDP-1B) do not show corresponding reductions in V_P and vice versa (e.g. 135-
456 140 m, DFDP-1B).

457

458 We explore this further using the following approach. In DFDP-1, V_P was measured
459 at 2 cm intervals using a single-source dual receiver logging sonde that estimates V_P
460 over a 30 cm interval (Townend et al., 2013). Therefore, by calculating the density of
461 damage zone structures using a moving average with a window size of 30 cm, we can
462 directly compare V_P to damage zone structure density for the DFDP-1 boreholes at
463 depth intervals of 2 cm. We follow the convention of Townend et al., (2013) who
464 noted that the resistivity anomaly associated with PSZ-1 in the DFDP-1B borehole is

465 at 128.4 m (Figure 8), which is 0.2 m below that measured in the drill-core. Therefore
466 the DFDP-1B drill-core depths are adjusted by 0.2 m downward. No correction is
467 required for DFDP-1A drill-core depths. It is noted that due to uncertainty in the core
468 depths, for example where there are intervals of no drill-core recovery, there may still
469 be a <30 cm difference between the corrected core depths and wireline log depths.

470

471 Cross-plots for all depths, and for depths separated by lithological unit, are shown in
472 Figure 10. Also shown is the 95% confidence interval (CI) for the slope of the best-fit
473 line to describe any correlation between damage zone structure density and V_p . In
474 cases where the CI's are both close to zero and positive (Figure 10a, b and e-g), a very
475 weak positive correlation exists. Where the CI's are either side of zero, there is no
476 statistically significant correlation between damage zone structure density and V_p
477 (Figure 10c and d). If we account for damage zone structures that are open or partially
478 open, only, then no significant correlation is also observed (Figure 10h). Thus we find
479 no systematic and consistent correlation between the elastic moduli of the fault rocks,
480 as measured by the V_p wireline logs of the DFDP-1 boreholes, and the density of
481 damage zone structures.

482

483 **5. Discussion**

484 An analysis of the distribution of damage zone structures around the Alpine Fault,
485 measured from DFDP-1 drill-core CT images and BHTV log data from the DFDP-1B
486 borehole (Townend et al., 2013; McNamara, 2015), is made here. These results are
487 then discussed in the context of other datasets gathered from the DFDP-1 project and
488 their interpretations (Sutherland et al., 2012; Townend et al., 2013; Carpenter et al.,

489 2014; Eccles et al., 2015; Toy et al., 2015), to inform how the damage zone may
490 influence various aspects of fault zone behaviour.

491

492 *5.1 On the density of damage zone structures with proximity to the fault core and*
493 *PSZs*

494 We find the highest density of damage zone structures in the shallowest core intervals
495 (39-45 m) in DFDP-1B (Figures 8). This is attributed to a high proportion of steeply-
496 dipping foliation-parallel fractures, relative to the rest of DFDP-1B core (Figure 11).
497 However, these fractures could conceivably have been generated from unloading
498 effects (Engelder, 1985; Zangerl et al., 2006), during the rapid exhumation of the
499 Alpine Fault hanging wall (Norris and Cooper, 2007). For this interval, their presence
500 could therefore mask a trend of increasing damage zone structure density towards the
501 fault.

502

503 For all other intervals sampled in DFDP-1, foliation-parallel fractures account for
504 only 11% of all damage zone structures. Consequently, uncertainty in whether this
505 fracture set reflects fault damage or unloading, will not affect our conclusion that the
506 density of damage zone structures does not increase with proximity to the PSZ or
507 fault core, within the scale of these intervals of DFDP-1 (30 m vertical distance in the
508 borehole both above and below the PSZs). It is still possible, though, that the density
509 of damage zone structures decays over a larger scale. Field studies, and coring from
510 deeper wells, which would provide a continued record of fracturing around the Alpine
511 Fault and span the transition from inside to outside the damage zone, would help
512 elucidate these observations.

513

514 The lack of decay in the density of damage zones sampled in the DFDP-1 CT images
515 is dissimilar to previous studies of fault damage zones that find clear decays in
516 fracture density with increasing distance from the fault core. Logarithmic (Chester et
517 al., 2005), exponential (Mitchell and Faulkner, 2009), and power law (Savage and
518 Brodsky, 2011; Johri et al., 2014) relationships have all been invoked to describe this
519 decay. Although McNamara, (2015) recognises a small degree of increasing damage
520 towards PSZ-1 in the BHTV logs of DFDP-1B (Figure 8), it is not as marked as has
521 been reported elsewhere.

522

523 *5.2 Lithological role on the Alpine Fault damage zone*

524 *5.2.1 Influence of lithology on the intensity of damage*

525 Though no relationship is found between the density of damage zone structures and
526 proximity to the PSZs within the scale of DFDP-1, we note some trends can be
527 modulated by lithology. For each of the lithological units defined by Toy et al.,
528 (2015), a representative example CT image of the unit and the density of damage zone
529 structures section is given in Figure 12. Unit 1 ultramylonites and the ‘2-4 mixture
530 unit’ contain the most damage zone structures. Unit 2 ultramylonites, which tend to be
531 sampled closer to the PSZs, contain fewer damage zone structures than unit 1
532 ultramylonites. The footwall cataclasite (unit 6) is cross cut by noticeably fewer
533 damage zone structures than the hanging wall cataclasites (unit 3 and 4). A link
534 between lithology and the intensity of damage zone structures has been described
535 elsewhere for faults in mixed sedimentary sequences (e.g. Chester & Logan 1986,
536 Peacock & Xing 1994, Berg & Skar 2005).

537

538 A lithological control on fracture density can be explained by the following. Ishii et
539 al., 2010 and Ishii, 2015 invoke that fractures are induced in damage zones during
540 fault slip by increasing differential stresses and/or decreasing effective normal
541 stresses, so that the Griffith-Coulomb failure criterion is met. Tensional strength (T_0),
542 frictional strength (μ) and cohesion (c) are fundamental constitutive properties of
543 lithology (Twiss and Moores, 2007; Ishii, 2015). Therefore, if variations existed in
544 these properties for the different units sampled in DFDP-1, the stresses (yield
545 strength) necessary for tensional, hybrid and/or shear fractures to form in each of
546 these units will also differ. Rheological variations associated with lithology will also
547 control fracturing since less competent rocks are more likely to respond to failure by
548 ductile shear deformation than by fracturing (Peacock and Xing, 1994; Fagereng and
549 Sibson, 2010; Rowe et al., 2013). Further aspects of damage zone formation may also
550 be influenced by lithology, such as the asymmetry of damage either side of a fault
551 (Ben-Zion and Shi, 2005; Dor et al., 2006), and the width of the damage zone (Beach
552 et al., 1999; Heynekamp et al., 1999).

553

554 *5.2.2 Lithological influence on the spatial distribution of damage zone structures* 555 *around DFDP-1*

556 Given our finding that lithology is systematically related to the density of damage
557 zone structures within the vicinity of the DFDP-1 boreholes, the distribution of the
558 lithologies will in turn control the distribution of damage zone structures. We find that
559 unit 1 ultramylonites that lie furthest from the Alpine Fault are the most heavily
560 damaged (Figure 13), though the degree with which this reflects seismic damage or
561 exhumation is unclear. With increasing proximity to the PSZs, a zone of interlayered

562 unit 2 ultramylonites, and unit 3 cataclasite units are encountered, as observed in
563 Figure 9. The PSZ itself is overlain by a ~10 m thick unit of foliated cataclasite (unit
564 4), in which the structures that define the damage zone are infrequent compared to
565 units 1-3. These observations indicate that with respect to Figure 1, the Alpine Fault
566 represents a composite of the two models. It has a central thick (~10 m) fault core
567 with well-defined PSZs (c.f. Figure 1a), but at its margins, fault core cataclasites
568 anastomose with damage zone units (c.f. Figure 1b). Below PSZ-1, lies unit 6
569 footwall cataclasite that exhibit few damage zone structures cross cutting the initial
570 cataclasite fabric (Figure 13).

571

572 Since damage zone structures are present within the fault core cataclasite units, where
573 they cross-cut its fabric (Figures 3b, c, 7, 8 and 11), the fault core and fault damage
574 zone spatially overlap. Damage is generated around the plane that accommodates
575 shear displacement (Cowie and Scholz, 1992; Andrews, 2005; Ben-Zion and Shi,
576 2005); thus at shallow depths where the frictional properties of the PSZ facilitate the
577 localisation of coseismic slip (Ikari et al., 2014), fracturing can occur within the
578 surrounding well-cemented cataclasites.

579

580 *5.3 Extent of fault zone healing*

581 As discussed in section 4.2, we find no consistent relationship between the density of
582 damage zone structures around the DFDP-1 boreholes and V_P as measured by
583 wireline logs of the DFDP-1 boreholes (Figure 10). This observation may be
584 interpreted in two ways: (1) in this study we only consider intermediate-macroscale
585 damage zone structures (aperture >1 mm), thus V_P may instead be controlled by

586 microfracture damage around the fault (e.g. Rempe et al. 2013), or (2) from healing of
587 fractures, at all scales since the last Alpine Fault earthquake, resulting in a negligible
588 effect of the fractures on the elastic moduli of the fault rocks and thus V_P .

589

590 We favour the latter explanation since evidence of widespread fracture healing is
591 found at both the macroscale in the CT images, and at the microscale, where a
592 pervasive calcite and clay cement, and relatively few open microfractures are noted
593 (Toy et al., 2015). Furthermore, laboratory elastic wave speed tests on cylindrical
594 samples from the DFDP-1 drill-core, whose dimensions (25 mm in diameter, <36 mm
595 long) dictate that they sample microfractures only, did not demonstrate a reduction in
596 V_P associated with microscale fracture density (Tatham et al., 2012; Carpenter et al.,
597 2014).

598

599 Even where open and partially open fractures are observed, they are not found to exert
600 an influence on V_P (Figure 10h); although it should be acknowledged that the lack of
601 filling in these fractures may not necessarily result from a lack of healing, but instead
602 from disturbance and opening during drilling. Nonetheless, it is clear that variations in
603 the elastic properties -and other petrophysical properties- of the rock mass
604 surrounding the DFDP-1 boreholes do not reflect fracturing, but instead changes in
605 the extent of alteration and comminution superimposed on differences in primary
606 lithology (Townend et al., 2013; Carpenter et al., 2014). This is in contrast to the San
607 Andreas Observatory at Depth borehole, where it is inferred that macro scale fractures
608 contribute to the development of a low velocity zone around the fault (Jeppson and
609 Tobin, 2015).

610

611 The concept of fault and fracture healing within the timescale of seismic cycles (10^1 -
612 10^4 years) has gathered much attention owing to its fundamental role in many models
613 for earthquake generation (Sibson, 1990; Rice, 1992; Chester et al., 1993).
614 Monitoring of fault zones immediately after an earthquake by seismic surveys (Li and
615 Vidale, 2001; Hiramatsu et al., 2005), or by studies of groundwater flow in boreholes
616 (Xue et al., 2013; Wästeby et al., 2014) report hydrochemical recovery initiating
617 immediately following an earthquake and that healing is complete within 2-10 years
618 of an earthquake. Laboratory measurements of permeability on drill-core recovered
619 approximately a year after the 1995 M_w 7.2 Kobe in Japan, show that despite fracture
620 filling noted in the drill-core itself (Lin et al., 2007), the damage zone is still an
621 interval of enhanced permeability (Lockner et al., 2009). This indicates that within a
622 year of an earthquake the damage zone is only partially healed. Laboratory studies,
623 which aim to recreate healing within natural fault zones, find these processes are
624 effective on timescales that range that from days to tens of years, depending on the
625 temperature and the chemistry of the pore fluid (Morrow et al., 2001; Tenthorey and
626 Cox, 2006). Field observations have also identified fracture sealing within the
627 recurrence intervals of large earthquakes (Woodcock et al., 2007). Since the Alpine
628 Fault last hosted a major rupture in 1717 AD (Wells et al., 1999; De Pascale and
629 Langridge, 2012), we conclude that in the intervening \sim 300 years, there has been
630 ample time for fracture healing to occur.

631

632 However, it is significant that this study considers the damage zone immediately
633 around the fault only (<30 m orthogonal distance from the PSZs). This interval lies
634 within the alteration zone, that is noted as a zone within which fractures have been

635 extensively healed (Sutherland et al., 2012). Outside the <50 m thick alteration zone,
636 drill-core recovery was low (Sutherland et al., 2011) with only 1.6 m of drill-core
637 recovered over a depth range of 7 m. This means we cannot directly compare fracture
638 healing inside and outside of the alteration zone using CT scans of DFDP-1 drill-core.

639

640 Nonetheless, the low drill-core recovery does indicate that this rock mass has low
641 geotechnical strength. This is an indicator that it contains more open fractures.
642 However, as noted in section 5.1, some of these fractures may have been generated by
643 mechanisms other than seismic damage. Further indirect evidence of less extensive
644 fracture healing outside the alteration zone comes from downhole permeability
645 measurements that record the highest permeability ($\sim 10^{-14} \text{ m}^{-2}$) in the damage zone
646 above the alteration zone (Sutherland et al., 2012), again suggesting the presence of
647 more open fractures in this interval. Thus, in the case of the Alpine Fault in its current
648 late interseismic state, the damage zone immediately adjacent to the fault core is not
649 the interval with the highest permeability.

650

651 This discrepancy in the extent to which fractures are healed inside and outside the
652 alteration zone of the Alpine Fault can contribute to our understanding of the
653 inconsistency between studies that report fracture healing and strength recovery
654 through seismic cycles (Moore et al., 1994; Morrow et al., 2001; Tenthorey et al.,
655 2003), and geophysical studies that find evidence of long-lived fracture induced
656 damage around faults (Cochran et al., 2009; Ellsworth and Malin, 2011). In the case
657 of the Alpine Fault, although fracture healing has occurred in the immediate vicinity
658 of the fault (within the alteration zone), healing did not universally affect the entire

659 damage zone. This allows damage-induced reduction in the elastic rigidity of rocks to
660 persist even though the Alpine Fault is late in its interseismic cycle, which thus
661 permits the propagation of Fault Zone Guided Waves, as reported within the Alpine
662 Fault by Eccles et al. (2015).

663

664 Determining the extent of fracture healing within a fault damage zone and its effect
665 on the elastic properties of the rock mass is important as unhealed fractures can rotate
666 the stress field around the fault (Faulkner et al., 2006; Gudmundsson et al., 2010),
667 increase the extent of seismic ruptures (Weng et al., 2016), and increase fault zone
668 compressibility which suppresses its ability to accommodate thermal pressurisation
669 (Griffith et al., 2009). In DFDP-1, interseismic healing has yielded a damage zone
670 that, immediately above (<50 m) the PSZs, has low permeability and high rigidity.
671 Coupled with a particular low PSZ permeability (Boulton et al., 2012; Sutherland et
672 al., 2012) this suggests that the conditions around the Alpine Fault are favourable for
673 thermal pressurisation to occur.

674

675 *5.4 Alpine Fault damage zone asymmetry*

676 Higher fracture densities have been observed in the hanging wall of a fault relative to
677 the footwall in several drilling projects into dipping thrust faults (Heermance et al.,
678 2003; Lin et al., 2007; Yeh et al., 2007; Li et al., 2013). Based on the relative
679 compliance of the rocks across the PSZs (Ben-Zion and Shi, 2005; Dor et al., 2006)
680 and its setting as a dipping thrust fault (Ma and Beroza, 2008; Ma, 2009), Townend et
681 al., (2013) predict that the extent of damage in the Alpine Fault will be greater in the
682 hanging wall, as it is relatively stiffer than the footwall.

683

684 Based on the CT images, we note that the unit 6 footwall cataclasites exhibit
685 relatively few damage zone structures that cross cut the cataclasite fabric compared to
686 the hanging wall units (Figure 12, Figure 13). This is consistent with the observations
687 of (Townend et al., 2013) and the analysis of fractures identified in the BHTV images
688 (McNamara, 2015).

689

690 Below the footwall cataclasites in DFDP-1B (i.e. at depths >143.85 m MD) a ~7 m
691 thick sequence of uncemented breccias were encountered; however it is not possible
692 to discriminate if brecciation was tectonic or drilling induced (Toy et al., 2015). As
693 they were not CT scanned these rocks have not been considered in this study.

694 Consequently, the full extent of the damage in the Alpine Fault footwall is still poorly
695 constrained and we cannot categorically state that the hanging wall is more damaged
696 than the footwall. Accounting for the bi-material effects on rupture dynamics and
697 damage zone asymmetry (Ben-Zion and Shi, 2005; Ma and Beroza, 2008) for the
698 Alpine Fault will require, but is worthy of, further study.

699

700 Finally, we note that these observations are based on two 1-D transects through a
701 heterogeneous fault system that exhibits variability along strike and with depth.
702 Future work characterising the Alpine Fault in the field will account for along strike
703 variation. A more complete assessment of damage at depth and damage in the
704 footwall would be particularly possible in future scientific drilling projects into the
705 Alpine Fault.

706

707 **6. Conclusions**

708 Qualitative and quantitative characterisation of structures that define the Alpine Fault
709 damage zone has been conducted using X-ray Computed Tomography (CT) scans of
710 drill-core recovered from the first phase of the Deep Fault Drilling Project (DFDP-1).
711 Statistical analysis of the density and distribution of these structures was performed
712 using a moving average that provides a more reliable measure of their distribution. A
713 weighting was also added that accounts for orientation bias. Our major findings, listed
714 below, are broadly consistent with independent analysis of damage zone structures
715 picked in BHTV logs of the DFDP-1B borehole (Townend et al., 2013; McNamara,
716 2015).

717 1. The density of damage zone structures does not increase with proximity to the
718 PSZs, within the scale of the DFDP-1 boreholes. Instead there is a lithological
719 influence on the density and distribution of damage zone structures.

720

721 2. Damage zone structures extends into the fault core cataclasites where they
722 cross cut the fabric. This is consistent with slip at shallow depths on Alpine
723 Fault occurring on the PSZs.

724

725 3. We find that the majority of the damage zone structures sampled in this study
726 are cemented/healed (72% fully, an additional 24% at least partially) by a
727 combination of clays, calcite and quartz. This is consistent with the fact that
728 the Alpine Fault is late in its interseismic cycle and has resulted in the
729 structures imparting no influence on the stiffness of the rocks as evidenced by

730 their P-wave velocity. This facilitates the conditions necessary for thermal
731 pressurisation to occur within the PSZ during earthquake rupture.

732

733 4. However, direct evidence of such damage zone healing is localised to within
734 <50 m of the Alpine Fault in the alteration zone. Outside this interval, there is
735 indirect evidence that fracture induced damage persists. Thus in the outer
736 damage zone, damage maybe a permanent feature of the Alpine Fault
737 throughout the seismic cycle

738

739 **Acknowledgements**

740 DFDP-1 was funded by: GNS Science; Victoria University of Wellington; the
741 University of Otago; the University of Auckland; the University of Canterbury;
742 Deutsche Forschungsgemeinschaft and the University of Bremen; Natural
743 Environment Research Council grants NE/J024449/1, NE/ G524160/1 and
744 NE/H012486/1 and the University of Liverpool; and the Marsden Fund of the Royal
745 Society of New Zealand. The International Continental Scientific Drilling Program,
746 ICDP (www.icdp-online.org) provided extensive support. JW was supported by a
747 University of Otago Doctoral Scholarship. We thank Steven Mills for his help in the
748 generation of unrolled CT images and Matthew Paris and the Oncology Department at
749 Dunedin Hospital for the use of a CT scanner. Reviews from James Kirkpatrick and
750 Marieke Rempe greatly improved this manuscript.

751

752 **References**

- 753 Anders, M.H., Wiltschko, D. V, 1994. Microfracturing, paleostress and the growth of
754 faults. *J. Struct. Geol.* 16, 795–815.
- 755 Andrews, D.J., 2005. Rupture dynamics with energy loss outside the slip zone. *J.*
756 *Geophys. Res. Solid Earth* 110.
- 757 Barton, C.A., Zoback, M.D., 1992. Self-similar distribution and properties of
758 macroscopic fractures at depth in crystalline rock in the Cajon Pass Scientific
759 Drill Hole. *J. Geophys. Res. Solid Earth* 97, 5181–5200.
- 760 Beach, A., Welbon, A.I., Brockbank, P.J., McCallum, J.E., 1999. Reservoir damage
761 around faults; outcrop examples from the Suez Rift. *Pet. Geosci.* 5, 109–116.
762 doi:10.1144/petgeo.5.2.109
- 763 Ben-Zion, Y., Shi, Z., 2005. Dynamic rupture on a material interface with
764 spontaneous generation of plastic strain in the bulk. *Earth Planet. Sci. Lett.* 236,
765 486–496.
- 766 Berg, S.S., Skar, T., 2005. Controls on damage zone asymmetry of a normal fault
767 zone: Outcrop analyses of a segment of the Moab fault, SE Utah. *J. Struct. Geol.*
768 27, 1803–1822. doi:10.1016/j.jsg.2005.04.012
- 769 Berryman, K.R., Cochran, U.A., Clark, K.J., Biasi, G.P., Langridge, R.M., Villamor,
770 P., 2012. Major earthquakes occur regularly on an isolated plate boundary fault.
771 *Science* (80-.). 336, 1690–1693.
- 772 Bistacchi, A., Massironi, M., Menegon, L., 2010. Three-dimensional characterization
773 of a crustal-scale fault zone: The Pusteria and Sprechenstein fault system
774 (Eastern Alps). *J. Struct. Geol.* 32, 2022–2041.
- 775 Bjørk, T.E., Mair, K., Austrheim, H., 2009. Quantifying granular material and

776 deformation: Advantages of combining grain size, shape, and mineral phase
777 recognition analysis. *J. Struct. Geol.* 31, 637–653. doi:10.1016/j.jsg.2009.03.020

778 Boulton, C., Carpenter, B.M., Toy, V., Marone, C., 2012. Physical properties of
779 surface outcrop cataclastic fault rocks, Alpine Fault, New Zealand.
780 *Geochemistry, Geophys. Geosystems.* doi:10.1029/2011gc003872

781 Boulton, C., Moore, D.E., Lockner, D.A., Toy, V.G., Townend, J., Sutherland, R.,
782 2014. Frictional properties of exhumed fault gouges in DFDP-1 cores, Alpine
783 Fault, New Zealand. *Geophys. Res. Lett.*

784 Caine, J.S., Evans, J.P., Forster, C.B., 1996. Fault zone architecture and permeability
785 structure. *Geology* 24, 1025–1028.

786 Carpenter, B.M., Kitajima, H., Sutherland, R., Townend, J., Toy, V.G., Saffer, D.M.,
787 2014. Hydraulic and acoustic properties of the active Alpine Fault, New Zealand:
788 Laboratory measurements on DFDP-1 drill core. *Earth Planet. Sci. Lett.* 390, 45–
789 51.

790 Chester, F.M., Chester, J.S., 2000. Stress and deformation along wavy frictional
791 faults. *J. Geophys. Res. Solid Earth* 105, 23421–23430.

792 Chester, F.M., Chester, J.S., 1998. Ultracataclasite structure and friction processes of
793 the Punchbowl fault, San Andreas system, California. *Tectonophysics* 295, 199–
794 221.

795 Chester, F.M., Evans, J.P., Biegel, R.L., 1993. Internal structure and weakening
796 mechanisms of the San Andreas fault. *J. Geophys. Res. Solid Earth* 98, 771–786.

797 Chester, F.M., Logan, J.M., 1986. Implications for mechanical properties of brittle
798 faults from observations of the Punchbowl fault zone, California. *Pure Appl.*
799 *Geophys. PAGEOPH* 124, 79–106. doi:10.1007/BF00875720

800 Chester, J.S., Chester, F.M., Kronenberg, A.K., 2005. Fracture surface energy of the
801 Punchbowl fault, San Andreas system. *Nature* 437, 133–136.

802 Childs, C., Manzocchi, T., Walsh, J.J., Bonson, C.G., Nicol, A., Schöpfer, M.P.J.,
803 2009. A geometric model of fault zone and fault rock thickness variations. *J.*
804 *Struct. Geol.* 31, 117–127.

805 Cochran, E.S., Li, Y.-G., Shearer, P.M., Barbot, S., Fialko, Y., Vidale, J.E., 2009.
806 Seismic and geodetic evidence for extensive, long-lived fault damage zones.
807 *Geology* 37, 315–318. doi:10.1130/G25306A.1

808 Columbus, J., Sirguey, P., Tenzer, R., 2011. A free fully assessed 15 metre digital
809 elevation model for New Zealand. *Surv. Q.* 300, 16.

810 Cooper, A.F., Norris, R.J., 1994. Anatomy, structural evolution, and slip rate of a
811 plate-boundary thrust: The Alpine fault at Gaunt Creek, Westland, New Zealand.
812 *Geol. Soc. Am. Bull.* 106, 627–633.

813 Cowie, P.A., Scholz, C.H., 1992. Physical explanation for the displacement-length
814 relationship of faults using a post-yield fracture mechanics model. *J. Struct.*
815 *Geol.* 14, 1133–1148.

816 De Pascale, G.P., Langridge, R.M., 2012. New on-fault evidence for a great
817 earthquake in A.D. 1717, central Alpine fault, New Zealand. *Geology.*
818 doi:10.1130/g33363.1

819 DeMets, C., Gordon, R.G., Argus, D.F., Stein, S., 1994. Effect of recent revisions to
820 the geomagnetic reversal time scale on estimates of current plate motions.
821 *Geophys. Res. Lett.* 21, 2191–2194.

822 Dor, O., Rockwell, T.K., Ben-Zion, Y., 2006. Geological observations of damage
823 asymmetry in the structure of the San Jacinto, San Andreas and Punchbowl faults

824 in southern California: A possible indicator for preferred rupture propagation
825 direction. *Pure Appl. Geophys.* 163, 301–349.

826 Eccles, J.D., Gulley, A.K., Malin, P.E., Boese, C.M., Townend, J., Sutherland, R.,
827 2015. Fault Zone Guided Wave Generation on the Locked, Late Interseismic
828 Alpine Fault, New Zealand. *Geophys. Res. Lett.*

829 Ellsworth, W.L., Malin, P.E., 2011. Deep rock damage in the San Andreas Fault
830 revealed by P-and S-type fault-zone-guided waves. *Geol. Soc. London, Spec.*
831 *Publ.* 359, 39–53.

832 Engelder, T., 1985. Loading paths to joint propagation during a tectonic cycle: an
833 example from the Appalachian Plateau, USA. *J. Struct. Geol.* 7, 459–476.

834 Fagereng, Å., Sibson, R.H., 2010. Melange rheology and seismic style. *Geology* 38,
835 751–754.

836 Faulkner, D.R., Jackson, C.A.L., Lunn, R.J., Schlische, R.W., Shipton, Z.K.,
837 Wibberley, C.J., Withjack, M.O., 2010. A review of recent developments
838 concerning the structure, mechanics and fluid flow properties of fault zones. *J.*
839 *Struct. Geol.* 32, 1557–1575.

840 Faulkner, D.R., Mitchell, T.M., Healy, D., Heap, M.J., 2006. Slip on “weak” faults by
841 the rotation of regional stress in the fracture damage zone. *Nature* 444, 922–925.

842 Faulkner, D.R., Mitchell, T.M., Jensen, E., Cembrano, J., 2011. Scaling of fault
843 damage zones with displacement and the implications for fault growth processes.
844 *J. Geophys. Res. Solid Earth* 116.

845 Faulkner, D.R., Mitchell, T.M., Rutter, E.H., Cembrano, J., 2008. On the structure
846 and mechanical properties of large strike-slip faults. *Geol. Soc. London, Spec.*
847 *Publ.* 299, 139–150.

848 Finzi, Y., Hearn, E.H., Ben-Zion, Y., Lyakhovsky, V., 2009. Structural properties and
849 deformation patterns of evolving strike-slip faults: Numerical simulations
850 incorporating damage rheology. *Pure Appl. Geophys.* 166, 1537–1573.

851 Fossen, H., Hesthammer, J., 2000. Possible absence of small faults in the Gullfaks
852 Field, northern North Sea: Implications for downscaling of faults in some porous
853 sandstones. *J. Struct. Geol.* 22, 851–863. doi:10.1016/S0191-8141(00)00013-4

854 Griffith, W.A., Sanz, P.F., Pollard, D.D., 2009. Influence of outcrop scale fractures on
855 the effective stiffness of fault damage zone rocks. *Pure Appl. Geophys.* 166,
856 1595–1627.

857 Gudmundsson, A., Simmenes, T.H., Larsen, B., Philipp, S.L., 2010. Effects of
858 internal structure and local stresses on fracture propagation, deflection, and arrest
859 in fault zones. *J. Struct. Geol.* 32, 1643–1655.

860 Heermance, R., Shipton, Z.K., Evans, J.P., 2003. Fault structure control on fault slip
861 and ground motion during the 1999 rupture of the Chelungpu fault, Taiwan. *Bull.*
862 *Seismol. Soc. Am.* 93, 1034–1050. doi:10.1785/0120010230

863 Heynekamp, M.R., Goodwin, L.B., Mozley, P.S., Haneberg, W.C., 1999. Controls on
864 Fault-Zone Architecture in Poorly Lithified Sediments, Rio Grande Rift, New
865 Mexico: Implications for Fault-Zone Permeability and Fluid Flow. *Faults*
866 *Subsurf. fluid flow shallow crust* 27–49.

867 Hiramatsu, Y., Honma, H., Saiga, A., Furumoto, M., Ooida, T., 2005. Seismological
868 evidence on characteristic time of crack healing in the shallow crust. *Geophys.*
869 *Res. Lett.* 32, 1–4. doi:10.1029/2005GL022657

870 Ikari, M.J., Carpenter, B.M., Kopf, A.J., Marone, C., 2014. Frictional strength, rate-
871 dependence, and healing in DFDP-1 borehole samples from the Alpine Fault,

872 New Zealand. Tectonophysics.

873 Ishii, E., 2015. Far-field stress dependency of the failure mode of damage-zone
874 fractures in fault zones: Results from laboratory tests and field observations of
875 siliceous mudstone. *J. Geophys. Res. Solid Earth*.

876 Ishii, E., Funaki, H., Tokiwa, T., Ota, K., 2010. Relationship between fault growth
877 mechanism and permeability variations with depth of siliceous mudstones in
878 northern Hokkaido, Japan. *J. Struct. Geol.* 32, 1792–1805.
879 doi:10.1016/j.jsg.2009.10.012

880 Jeanne, P., Guglielmi, Y., Cappa, F., 2012. Multiscale seismic signature of a small
881 fault zone in a carbonate reservoir: Relationships between V P imaging, fault
882 zone architecture and cohesion. *Tectonophysics* 554, 185–201.

883 Jeppson, T.N., Bradbury, K.K., Evans, J.P., 2010. Geophysical properties within the
884 San Andreas Fault Zone at the San Andreas Fault Observatory at Depth and their
885 relationships to rock properties and fault zone structure. *J. Geophys. Res. Solid*
886 *Earth* 115.

887 Jeppson, T.N., Tobin, H.J., 2015. San Andreas Fault Zone velocity structure at
888 SAFOD at core, log, and seismic scales. *J. Geophys. Res. Solid Earth*.

889 Johri, M., Zoback, M.D., Hennings, P., 2014. A scaling law to characterize fault
890 damage zones at reservoir depths. *Am. Assoc. Pet. Geol. Bull.*

891 Keren, T.T., Kirkpatrick, J.D., 2016. Data report: tectonic and induced structures in
892 the JFAST core, in: *Proc. IODP| Volume*. p. 343T.

893 Ketcham, R.A., Carlson, W.D., 2001. Acquisition, optimization and interpretation of
894 X-ray computed tomographic imagery: applications to the geosciences. *Comput.*
895 *Geosci.* 27, 381–400.

896 Kulander, B.R., Dean, S.L., Ward, B.J., 1990. Fractured core analysis: interpretation,
897 logging, and use of natural and induced fractures in core. American Association
898 of Petroleum Geologists.

899 Lachenbruch, A.H., 1980. Frictional heating, fluid pressure, and the resistance to fault
900 motion. *J. Geophys. Res* 85, 6097–6112.

901 Li, H., Wang, H., Xu, Z., Si, J., Pei, J., Li, T., Huang, Y., Song, S.-R., Kuo, L.-W.,
902 Sun, Z., 2013. Characteristics of the fault-related rocks, fault zones and the
903 principal slip zone in the Wenchuan Earthquake Fault Scientific Drilling Project
904 Hole-1 (WFSD-1). *Tectonophysics* 584, 23–42.

905 Li, Y., Vidale, J.E., 2001. Healing of the shallow fault zone from 1994–1998 after the
906 1992 M7. 5 Landers, California, earthquake. *Geophys. Res. Lett.* 28, 2999–3002.

907 Lin, A., Maruyama, T., Kobayashi, K., 2007. Tectonic implications of damage zone-
908 related fault-fracture networks revealed in drill core through the Nojima fault,
909 Japan. *Tectonophysics* 443, 161–173.

910 Lin, A., Yamashita, K., 2013. Spatial variations in damage zone width along strike-
911 slip faults: An example from active faults in southwest Japan. *J. Struct. Geol.* 57,
912 1–15.

913 Lockner, D. a., Tanaka, H., Ito, H., Ikeda, R., Omura, K., Naka, H., 2009. Geometry
914 of the Nojima Fault at Nojima-Hirabayashi, Japan – I. A Simple Damage
915 Structure Inferred from Borehole Core Permeability. *Pure Appl. Geophys.* 166,
916 1649–1667. doi:10.1007/s00024-009-0515-0

917 Lund Snee, J.-E., Toy, V.G., Gessner, K., 2014. Significance of brittle deformation in
918 the footwall of the Alpine Fault, New Zealand: Smithy Creek Fault zone. *J.*
919 *Struct. Geol.* 64, 79–98.

- 920 Ma, S., 2009. Distinct asymmetry in rupture-induced inelastic strain across dipping
921 faults: An off-fault yielding model. *Geophys. Res. Lett.* 36.
- 922 Ma, S., Beroza, G.C., 2008. Rupture dynamics on a bimaterial interface for dipping
923 faults. *Bull. Seismol. Soc. Am.* 98, 1642–1658.
- 924 Massiot, C., McNamara, D.D., Lewis, B., 2015. Processing and analysis of high
925 temperature geothermal acoustic borehole image logs in the Taupo Volcanic
926 Zone, New Zealand. *Geothermics* 53, 190–201.
- 927 Mauldon, M., Dunne, W.M., Rohrbaugh, M.B., 2001. Circular scanlines and circular
928 windows: New tools for characterizing the geometry of fracture traces. *J. Struct.*
929 *Geol.* 23, 247–258. doi:10.1016/S0191-8141(00)00094-8
- 930 McNamara, D., 2015. Exploring New Zealand's subsurface using borehole images,
931 in: Presented at the 2015 New Zealand GeoSciences Conference, Wellington,
932 25-27th November (2015).
- 933 Mitchell, T.M., Faulkner, D.R., 2012. Towards quantifying the matrix permeability of
934 fault damage zones in low porosity rocks. *Earth Planet. Sci. Lett.* 339, 24–31.
- 935 Mitchell, T.M., Faulkner, D.R., 2009. The nature and origin of off-fault damage
936 surrounding strike-slip fault zones with a wide range of displacements: a field
937 study from the Atacama fault system, northern Chile. *J. Struct. Geol.* 31, 802–
938 816.
- 939 Mitchell, T.M., Toy, V.G., 2014. Photograph of the month. *J. Struct. Geol.* 64, iii.
940 doi:10.1016/S0191-8141(14)00094-7
- 941 Moore, D.E., Lockner, D.A., Byerlee, J.D., 1994. Reduction of permeability in granite
942 at elevated temperatures. *Science* (80-.). 265, 1558–1561.
- 943 Morrow, C.A., Moore, D.E., Lockner, D.A., 2001. Permeability reduction in granite

944 under hydrothermal conditions. *J. Geophys. Res. Solid Earth* 106, 30551–30560.

945 Norris, R.J., Cooper, A.F., 2007. The Alpine Fault, New Zealand: surface geology
946 and field relationships, in: Okaya, D., Stern, T.A., Davey, F. (Eds.), A
947 Continental Plate Boundary: Tectonics at South Island, New Zealand. American
948 Geophysical Union, pp. 157–175.

949 Norris, R.J., Cooper, A.F., 2001. Late Quaternary slip rates and slip partitioning on
950 the Alpine Fault, New Zealand. *J. Struct. Geol.* 23, 507–520.

951 Norris, R.J., Cooper, A.F., 1997. Erosional control on the structural evolution of a
952 transpressional thrust complex on the Alpine Fault, New Zealand. *J. Struct. Geol.*
953 19, 1323–1342.

954 Peacock, D.C.P., Xing, Z., 1994. Field examples and numerical modelling of
955 oversteps and bends along normal faults in cross-section. *Tectonophysics*.
956 doi:10.1016/0040-1951(94)90209-7

957 Priest, S.D., 1993. Discontinuity analysis for rock engineering. Springer Science &
958 Business Media.

959 Reed, J.J., 1964. Mylonites, cataclasites, and associated rocks along the Alpine fault,
960 South Island, New Zealand. *New Zeal. J. Geol. Geophys.* 7, 645–684.

961 Rempe, M., Mitchell, T., Renner, J., Nippres, S., Ben-Zion, Y., Rockwell, T., 2013.
962 Damage and seismic velocity structure of pulverized rocks near the San Andreas
963 Fault. *J. Geophys. Res. Solid Earth* 118, 2813–2831.

964 Rice, J.R., 1992. Fault Stress States, Pore Pressure Distributions, and the Weakness of
965 the San Andreas Fault. *Fault Mech. Transp. Prop. Rocks*.

966 Rice, J.R., Sammis, C.G., Parsons, R., 2005. Off-fault secondary failure induced by a
967 dynamic slip pulse. *Bull. Seismol. Soc. Am.* 95, 109–134.

968 Rowe, C.D., Moore, J.C., Remitti, F., 2013. The thickness of subduction plate
969 boundary faults from the seafloor into the seismogenic zone. *Geology* 41, 991–
970 994.

971 Savage, H.M., Brodsky, E.E., 2011. Collateral damage: Evolution with displacement
972 of fracture distribution and secondary fault strands in fault damage zones. *J.*
973 *Geophys. Res. Solid Earth* 116.

974 Savage, H.M., Cooke, M.L., 2010. Unlocking the effects of friction on fault damage
975 zones. *J. Struct. Geol.* 32, 1732–1741.

976 Schulz, S.E., Evans, J.P., 2000. Mesoscopic structure of the Punchbowl Fault,
977 Southern California and the geologic and geophysical structure of active strike-
978 slip faults. *J. Struct. Geol.* 22, 913–930.

979 Schulz, S.E., Evans, J.P., 1998. Spatial variability in microscopic deformation and
980 composition of the Punchbowl fault, southern California: Implications for
981 mechanisms, fluid-rock interaction, and fault morphology. *Tectonophysics* 295,
982 223–244. doi:10.1016/S0040-1951(98)00122-X

983 Sibson, R.H., 1990. Conditions for fault-valve behaviour. *Geol. Soc. London, Spec.*
984 *Publ.* 54, 15–28.

985 Sibson, R.H., 1977. Fault rocks and fault mechanisms. *J. Geol. Soc. London.* 133,
986 191–213. doi:10.1144/gsjgs.133.3.0191

987 Sibson, R.H., 1973. Interactions between Temperature and Pore-Fluid Pressure during
988 Earthquake Faulting and a Mechanism for Partial or Total Stress Relief. *Nat.*
989 *Phys. Sci.* 243, 66–68.

990 Sibson, R.H., White, S.H., Atkinson, B.K., 1981. Structure and distribution of fault
991 rocks in the Alpine Fault Zone, New Zealand. *Geol. Soc. London, Spec. Publ.* 9,

992 197–210.

993 Stierman, D.J., Kovach, R.L., 1979. An in situ velocity study: the Stone Canyon well.
994 J. Geophys. Res. Solid Earth 84, 672–678.

995 Storti, F., Balsamo, F., Salvini, F., 2007. Particle shape evolution in natural carbonate
996 granular wear material. Terra Nov. 19, 344–352. doi:10.1111/j.1365-
997 3121.2007.00758.x

998 Sutherland, R., Eberhart-Phillips, D., Harris, R.A., Stern, T., Bevan, J., Ellis, S.,
999 Henrys, D., Cox, S., Norris, R.J., Berryman, K.R., Townend, J., Bannister, S.,
1000 Pettinga, J., Leitner, B., Wallace, L., Little, T.A., Cooper, A.F., Yetton, M.,
1001 Stirling, M., 2007. Do great earthquakes occur on the Alpine Fault in central
1002 South Island, New Zealand?, A Continental Plate Boundary: Tectonics at South
1003 Island, New Zealand; AGU Geophysical Monograph.

1004 Sutherland, R., Toy, V., Townend, J., Eccles, J., Prior, D.J., Norris, R.J., Mariani, E.,
1005 Faulkner, D.R., de Pascale, G., Carpenter, B.M., Boulton, C., Menzies, C.D.,
1006 Cox, S., 2011. Operations and well completion report for boreholes DFDP-1A
1007 and DFDP-1B, Deep Fault Drilling Project, Alpine Fault, Gaunt Creek, New
1008 Zealand.

1009 Sutherland, R., Toy, V.G., Townend, J., Cox, S.C., Eccles, J.D., Faulkner, D.R., Prior,
1010 D.J., Norris, R.J., Mariano, R., Boulton, C., Carpenter, B.M., Menzies, C.D.,
1011 Little, T.A., Hasting, M., De Pascale, G.P., Langridge, R.M., Scott, H.R., Reid
1012 Lindroos, Z., Fleming, B., Kopf, A.J., 2012. Drilling reveals fluid control on
1013 architecture and rupture of the Alpine Fault, New Zealand, Geology.

1014 Tatham, D.J., Faulkner, D.R., Mariani, E., Toy, V.G., 2012. Laboratory
1015 measurements of the permeability and P and S wave velocity and anisotropy of

1016 rocks from DFDP-1A, Alpine fault zone, New Zealand, in: AGU Fall Meeting
1017 Abstracts. p. 2615.

1018 Tenthorey, E., Cox, S.F., 2006. Cohesive strengthening of fault zones during the
1019 interseismic period: An experimental study. *J. Geophys. Res. Solid Earth* 111.

1020 Tenthorey, E., Cox, S.F., Todd, H.F., 2003. Evolution of strength recovery and
1021 permeability during fluid–rock reaction in experimental fault zones. *Earth Planet.*
1022 *Sci. Lett.* 206, 161–172.

1023 Terzaghi, R.D., 1965. Sources of error in joint surveys. *Geotechnique* 15, 287–304.

1024 Townend, J., Sutherland, R., Toy, V., 2009. Deep Fault Drilling Project-Alpine Fault,
1025 New Zealand, Scientific Drilling.

1026 Townend, J., Sutherland, R., Toy, V.G., Eccles, J.D., Boulton, C., Cox, S.C.,
1027 McNamara, D., 2013. Late-interseismic state of a continental plate-bounding
1028 fault: Petrophysical results from DFDP-1 wireline logging and core analysis,
1029 Alpine Fault, New Zealand. *Geochemistry, Geophys. Geosystems* 14, 3801–
1030 3820.

1031 Toy, V., 2008. Rheology of the Alpine Fault mylonite zone: deformation processes at
1032 and below the base of the seismogenic zone in a major plate boundary structure.
1033 University of Otago.

1034 Toy, V.G., Boulton, C.J., Sutherland, R.S., Townend, J., Norris, R.J., Little, T.A.,
1035 Prior, D.J., Mariani, E., Faulkner, D.R., Menzies, C.D., Scott, H.R., Carpenter,
1036 B.M., 2015. Fault rock lithologies and architecture of the central Alpine Fault,
1037 New Zealand, revealed by DFDP-1 drilling.

1038 Twiss, R.J., Moores, E.M., 2007. *Structural Geology*, 736 pp.

1039 Vermilye, J.M., Scholz, C.H., 1998. The process zone: A microstructural view of fault

1040 growth. *J. Geophys. Res. Solid Earth* 103, 12223–12237.

1041 Wallace, L.M., Beavan, J., McCaffrey, R., Berryman, K., Denys, P., 2007. Balancing
1042 the plate motion budget in the South Island, New Zealand using GPS, geological
1043 and seismological data. *Geophys. J. Int.* 168, 332–352.

1044 Wand, M.P., 1997. Data-based choice of histogram bin width. *Am. Stat.* 51, 59–64.

1045 Warr, L.N., Cox, S.C., 2001. Clay mineral transformations and weakening
1046 mechanisms along the Alpine Fault, New Zealand, in: Holdsworth, R.E.,
1047 Strachan, R.A., Magloughlin, J.F., Knipe, R.J. (Eds.), *The Nature and Tectonic
1048 Significance of Fault Zone Weakening*. The Geological Society, London, pp. 85–
1049 101.

1050 Wästeby, N., Skelton, A., Tollefsen, E., Andrén, M., Stockmann, G., Liljedahl, L.C.,
1051 Sturkell, E., Mörth, M., 2014. Hydrochemical monitoring, petrological
1052 observation and geochemical modelling of fault healing after an earthquake. *J.
1053 Geophys. Res. Solid Earth*.

1054 Watkins, H., Bond, C.E., Healy, D., Butler, R.W.H., 2015. Appraisal of fracture
1055 sampling methods and a new workflow to characterise heterogeneous fracture
1056 networks at outcrop. *J. Struct. Geol.* 72, 67–82.

1057 Wells, A., Yetton, M.D., Duncan, R.P., Stewart, G.H., 1999. Prehistoric dates of the
1058 most recent Alpine fault earthquakes, New Zealand. *Geology* 27, 995–998.

1059 Weng, H., Yang, H., Zhang, Z., Chen, X., 2016. Earthquake rupture extents and
1060 coseismic slips promoted by damaged fault zones. *J. Geophys. Res. Solid Earth*.

1061 Wennberg, O.P., Rennan, L., Basquet, R., 2009. Computed tomography scan imaging
1062 of natural open fractures in a porous rock; geometry and fluid flow. *Geophys.
1063 Prospect.* 57, 239–249.

1064 Wibberley, C.A.J., Shimamoto, T., 2003. Internal structure and permeability of major
1065 strike-slip fault zones: the Median Tectonic Line in Mie Prefecture, Southwest
1066 Japan. *J. Struct. Geol.* 25, 59–78.

1067 Wibberley, C.A.J., Yielding, G., Di Toro, G., 2008. Recent advances in the
1068 understanding of fault zone internal structure: A review. *Geol. Soc. London,*
1069 *Spec. Publ.* 299, 5–33.

1070 Wilson, J.E., Chester, J.S., Chester, F.M., 2003. Microfracture analysis of fault
1071 growth and wear processes, Punchbowl Fault, San Andreas system, California. *J.*
1072 *Struct. Geol.* 25, 1855–1873.

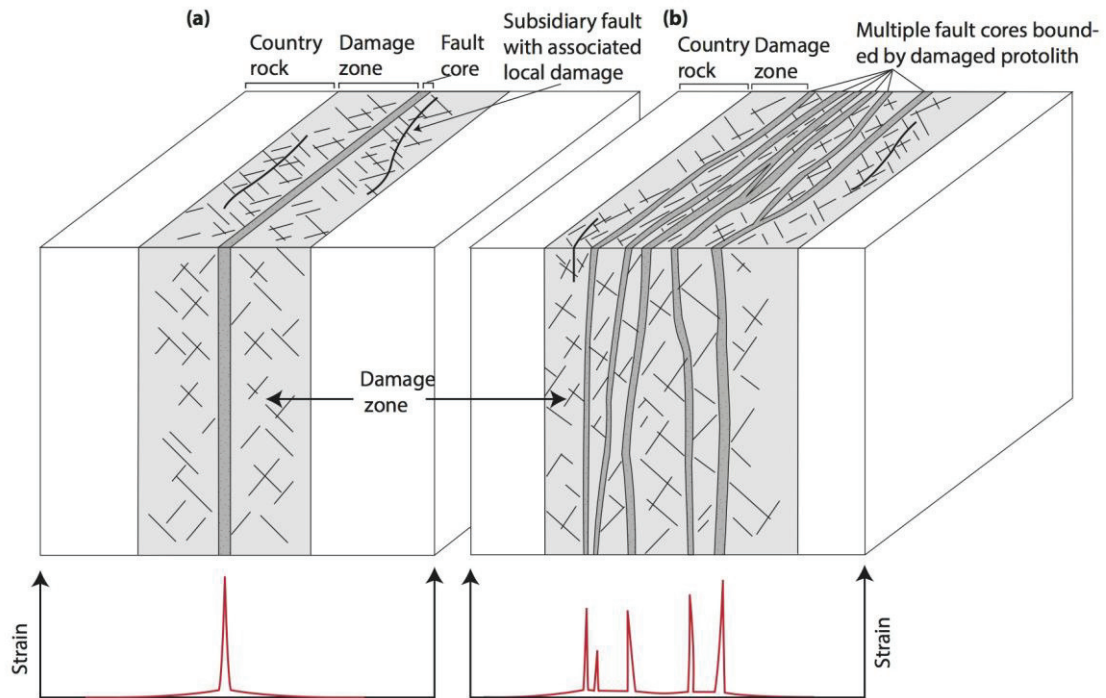
1073 Woodcock, N.H., Dickson, J.A.D., Tarasewicz, J.P.T., 2007. Transient permeability
1074 and reseal hardening in fault zones: evidence from dilation breccia textures.
1075 *Geol. Soc. London, Spec. Publ.* 270, 43–53.

1076 Xue, L., Li, H.-B., Brodsky, E.E., Xu, Z.-Q., Kano, Y., Wang, H., Mori, J.J., Si, J.-L.,
1077 Pei, J.-L., Zhang, W., Yang, G., Sun, Z.-M., Huang, Y., 2013. Continuous
1078 permeability measurements record healing inside the Wenchuan earthquake fault
1079 zone. *Science* 340, 1555–9. doi:10.1126/science.1237237

1080 Yeh, E.-C., Sone, H., Nakaya, T., Ian, K.-H., Song, S.-R., Hung, J.-H., Lin, W.,
1081 Hirono, T., Wang, C.-Y., Ma, K.-F., 2007. Core description and characteristics
1082 of fault zones from Hole-A of the Taiwan Chelungpu-Fault Drilling Project.
1083 *Terr. Atmos. Ocean. Sci.* 18, 327–357.

1084 Zangerl, C., Loew, S., Eberhardt, E., 2006. Structure, geometry and formation of
1085 brittle discontinuities in anisotropic crystalline rocks of the central Gotthard
1086 massif, Switzerland. *Eclogae Geol. Helv.* 99, 271–290. doi:10.1007/s00015-006-
1087 1190-0

1088

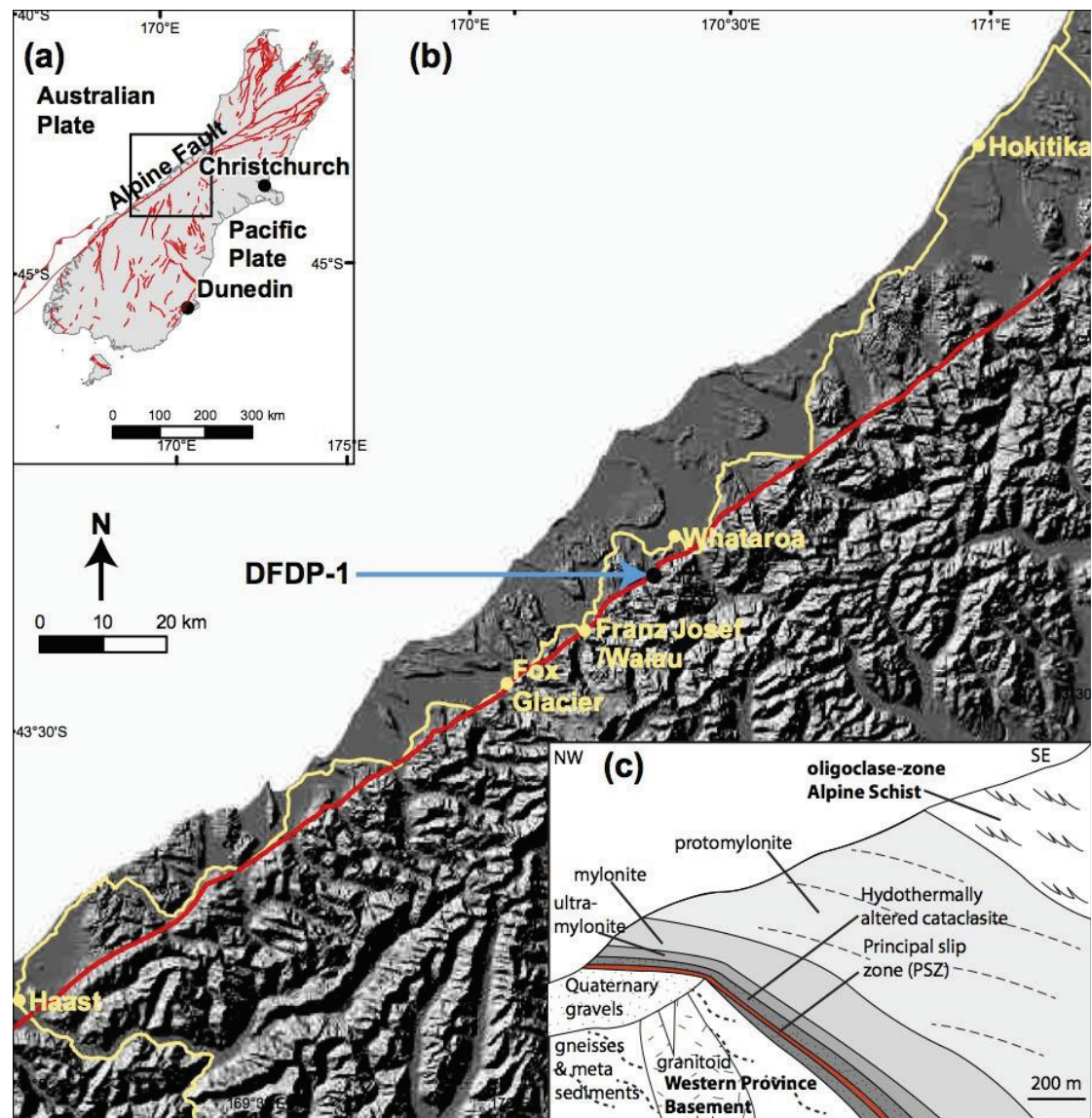
1 **Figure 1**

2

3 Figure 1: Conceptual models of fault zone architecture with different configurations
 4 of damage zone and fault core: (a) single fault core, and (b) multiple anastomosing
 5 fault cores bounded by lenses of damaged rock. A schematic representation of how
 6 brittle strain may be distributed across these faults is also shown. Diagram
 7 intentionally has no scale. Modified from Mitchell and Faulkner (2009).

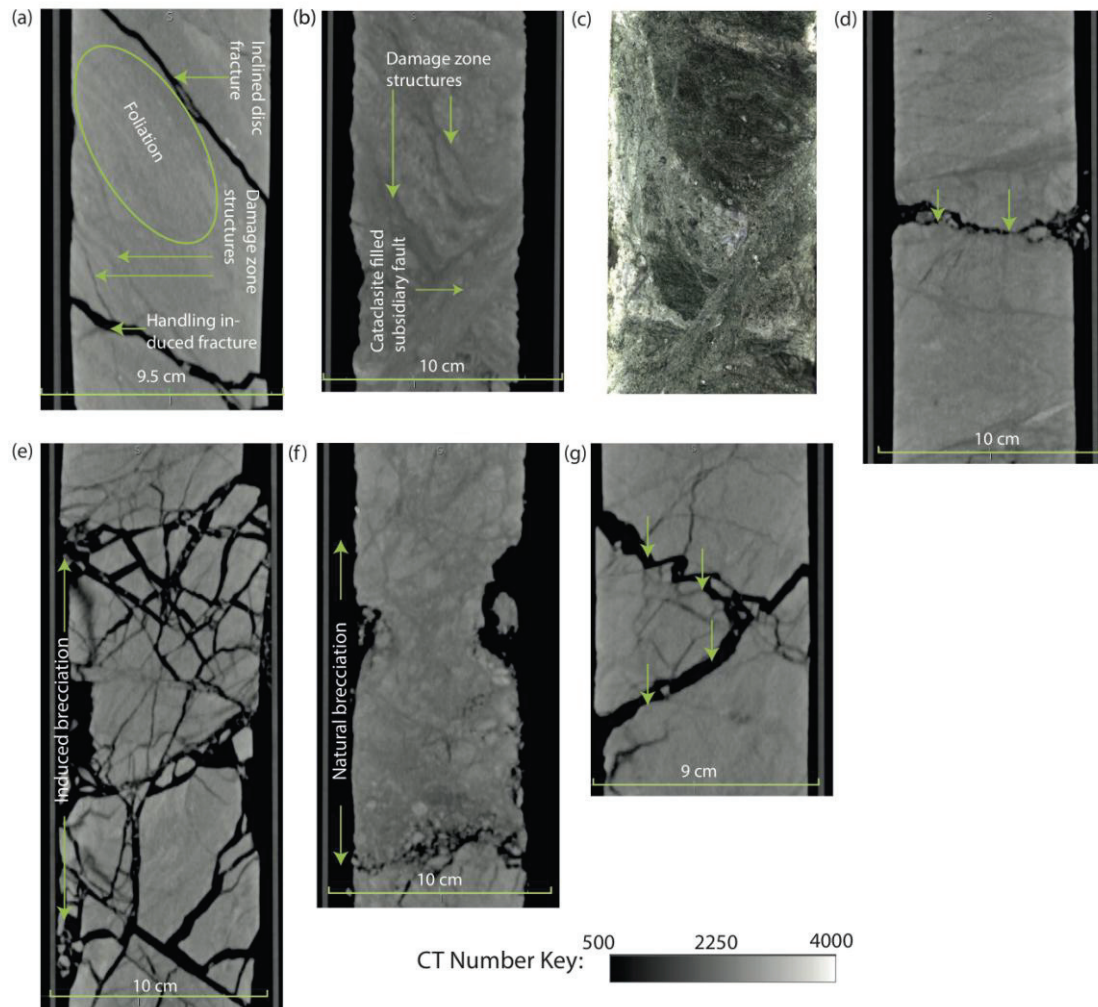
8

1 Figure 2



2
3 Figure 2: Location map. (a) Map of South Island, New Zealand showing extent of
4 Alpine Fault and all other onshore active faults for South Island (GNS Active Fault
5 Database, <http://data.gns.cri.nz/af/>). Black box illustrates extent of (b), a locality map
6 for the DFDP-1 site at Gaunt Creek in the context of the central section of the Alpine
7 Fault (red line) that extends roughly between Hokitika and Haast. Hills illuminated
8 using greyscale from 15 m digital elevation model (Columbus et al., 2011),
9 illumination is from the northwest, yellow lines are roads. (c) Composite schematic

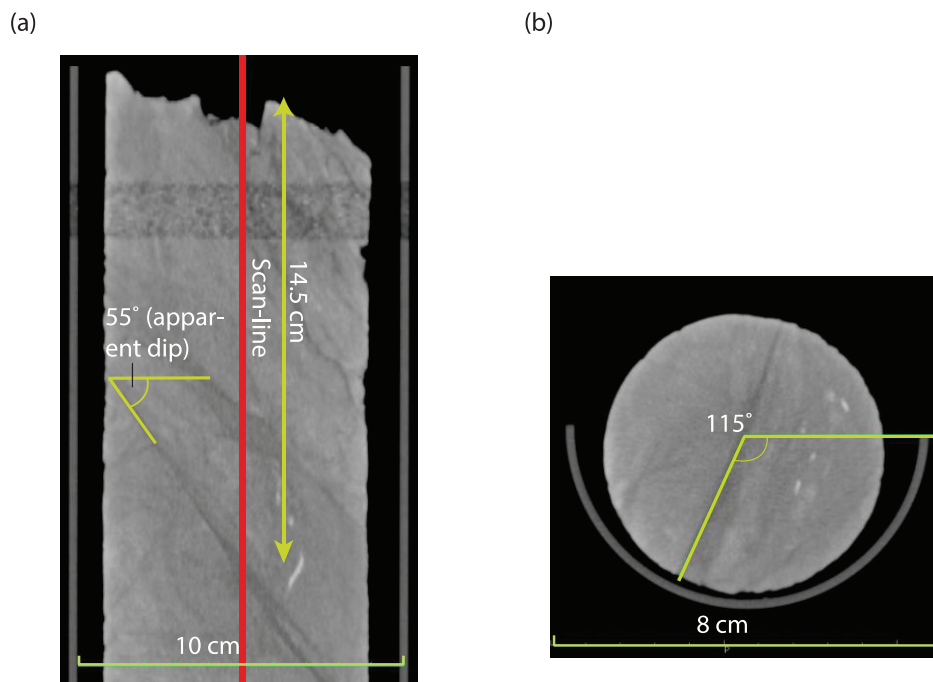
- 10 section of rock sequence typically encountered in an oblique thrust segment of the
- 11 central Alpine Fault, modified after Norris and Cooper (2007).

1 **Figure 3**

2

3 Figure 3: Distinction between damage zone structures and other features in 2D X-ray
 4 computed tomography (CT) images. (a) CT drill-core axial parallel image of DFDP-1
 5 drill-core (1B-34-1 101.97-102.13 m). Whilst foliation and fractures both appear as
 6 linear arrangement of anomalous CT values, fractures have more distinct boundaries
 7 and greater anomalies of CT values. The foliation-parallel black fracture is interpreted
 8 to have formed from the release of confining pressure during the drilling itself, whilst
 9 the sub-horizontal black fracture is noted in the core-log as being handling induced.
 10 (b) CT image and (c) equivalent section in 180° core scan, to show examples of
 11 damage zone structures in a cataclasite unit (DFDP-1B 66-1 138.38-138.56 m), in

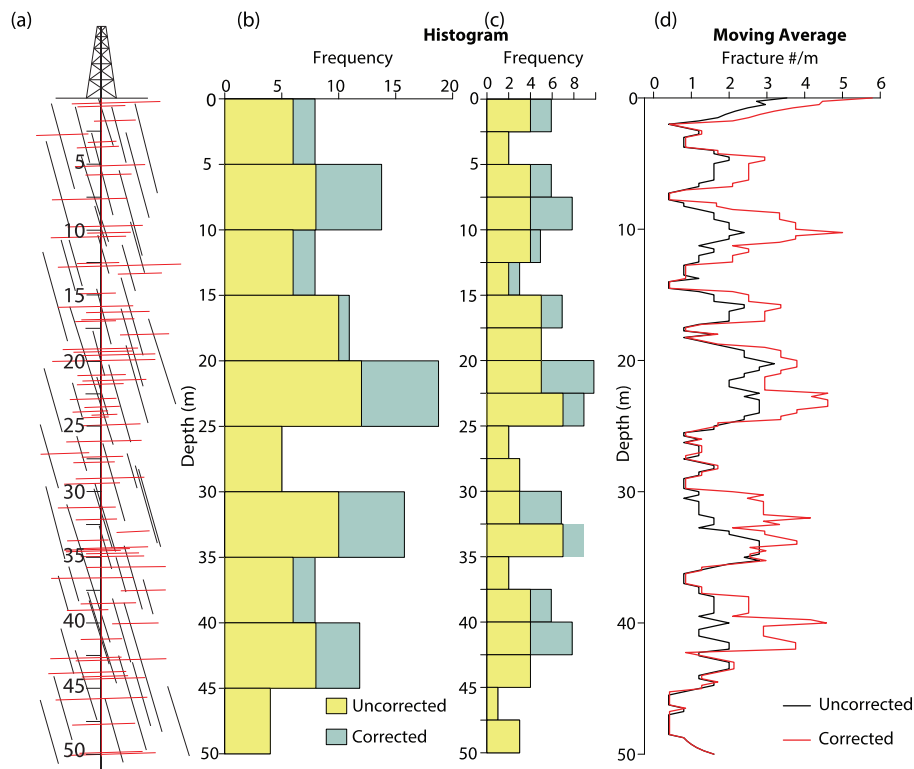
12 which fractures and subsidiary faults cross cut the initial cataclasite fabric. (d) Disc
13 fracture in DFDP-1A 60-2 81.50-81.70 m. Example of core sections with induced (e,
14 DFDP-1A 49-1 67.7-67.95 m) and natural (f, DFDP-1B 31-1 96.75-96.95 m)
15 brecciation. Induced brecciation is characterised by angular fragmentation of the core,
16 during drilling, whereas natural brecciation leads to the rounding of clasts. (g) Two
17 open fractures dipping in opposite directions to define a triangular set whose apex
18 points at the centre of the drill-core (DFDP-1A 54-1 73.7-73.83 m). CT numbers refer
19 to greyscale as shown. This greyscale is used in all subsequent CT images.

1 **Figure 4**

2

3 Figure 4: (a) Example of how the depth of a dipping damage zone structure was
 4 measured by recording the depth at which the structure intersected a scan-line parallel
 5 to the core axis in a 2D CT image (1B-37-2 105.96-106.15 m). Depth is measured
 6 relative to the top of the core section; these sections are registered to absolute depths
 7 so from them the depth of the structure within the borehole can be calculated. (b) To
 8 measure the orientation of a damage zone structure within a local core reference
 9 frame; strike was measured in a CT axial slice image of the core (which represents a
 10 horizontal plane since the DFDP-1 boreholes were vertical) relative to the right hand
 11 edge of the core container, which was denoted 'north.' An apparent dip of the
 12 structure was measured from the angle between the damage zone structure and a line
 13 90° to the core axis in a core axial parallel 2D CT scan image as shown in (a). Using
 14 the strike, a true dip can then be calculated from apparent dip

15

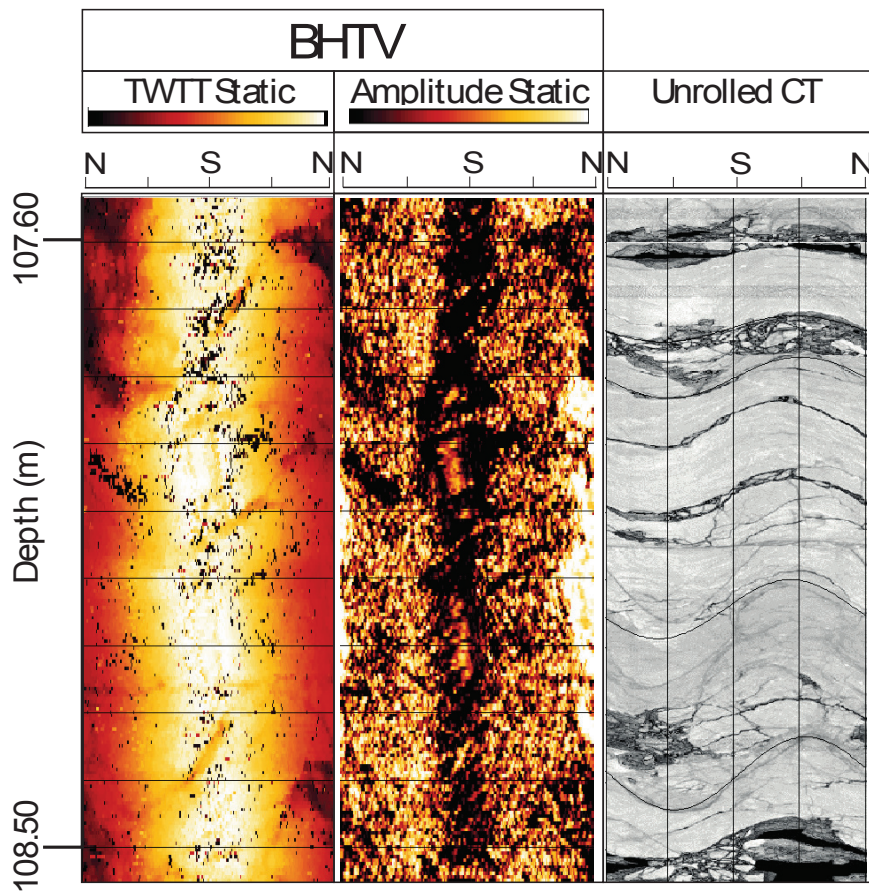
1 **Figure 5**

2

3

4 Figure 5: (a) A hypothetical fractured rock mass intersected by a vertical borehole,
 5 illustrating how fracture density and distribution may be calculated in a borehole. The
 6 rock mass contains two fracture sets: (1) dipping at 03° (red) and (2) dipping at 70°
 7 (black). These intersect the borehole at a randomly generated set of depths using the
 8 ‘sample’ function in the statistical programming language R ([https://stat.ethz.ch/R-](https://stat.ethz.ch/R-manual/R-devel/library/base/html/sample.html)
 9 [manual/R-devel/library/base/html/sample.html](https://stat.ethz.ch/R-manual/R-devel/library/base/html/sample.html)). (b&c) Fracture distribution around
 10 the borehole represented using a histogram with frequency calculated in (b) 5 m bins
 11 and (c) 2.5 m bins. Blue boxes in histograms represent fracture density calculated
 12 using the Terzaghi correction for orientation bias as explained in text. (d) Fracture set
 13 depicted using a (black) moving and (red) weighted moving average calculation,
 14 which are uncorrected and corrected orientation bias respectively. Moving average

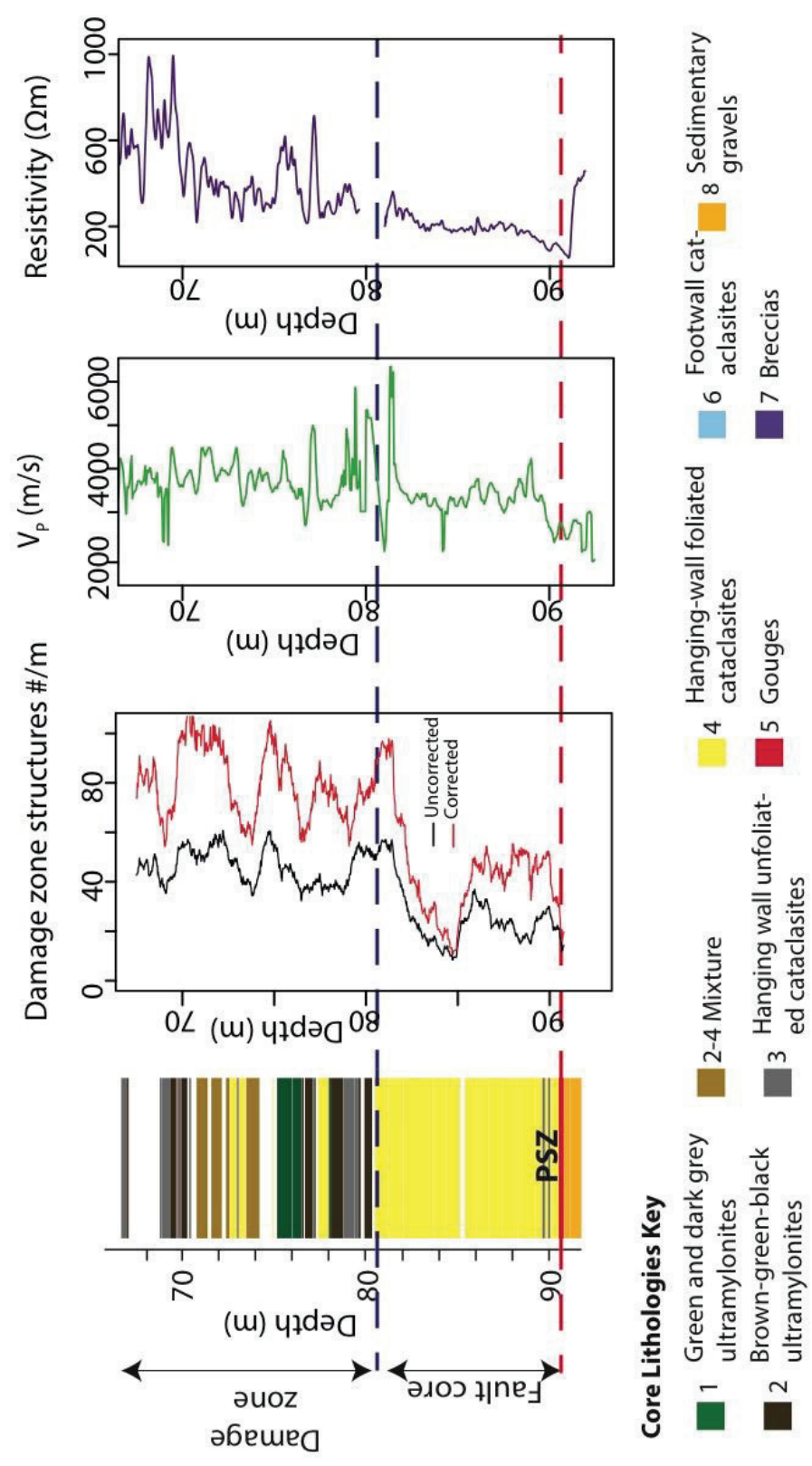
15 has been calculated using a moving window of 2.5 m and at intervals of 25 cm. When
16 fracture density is represented using a moving average it gives a better representation
17 of intervals of high fracture density that are split across two bins (such as at ~10 m)
18 than when fracture density is represented on a histogram. Introducing a weighting to
19 correct for orientation bias gives a better representation of the density of steeply
20 dipping fractures in the rock mass but does not inform us further on their distribution.

1 **Figure 6**

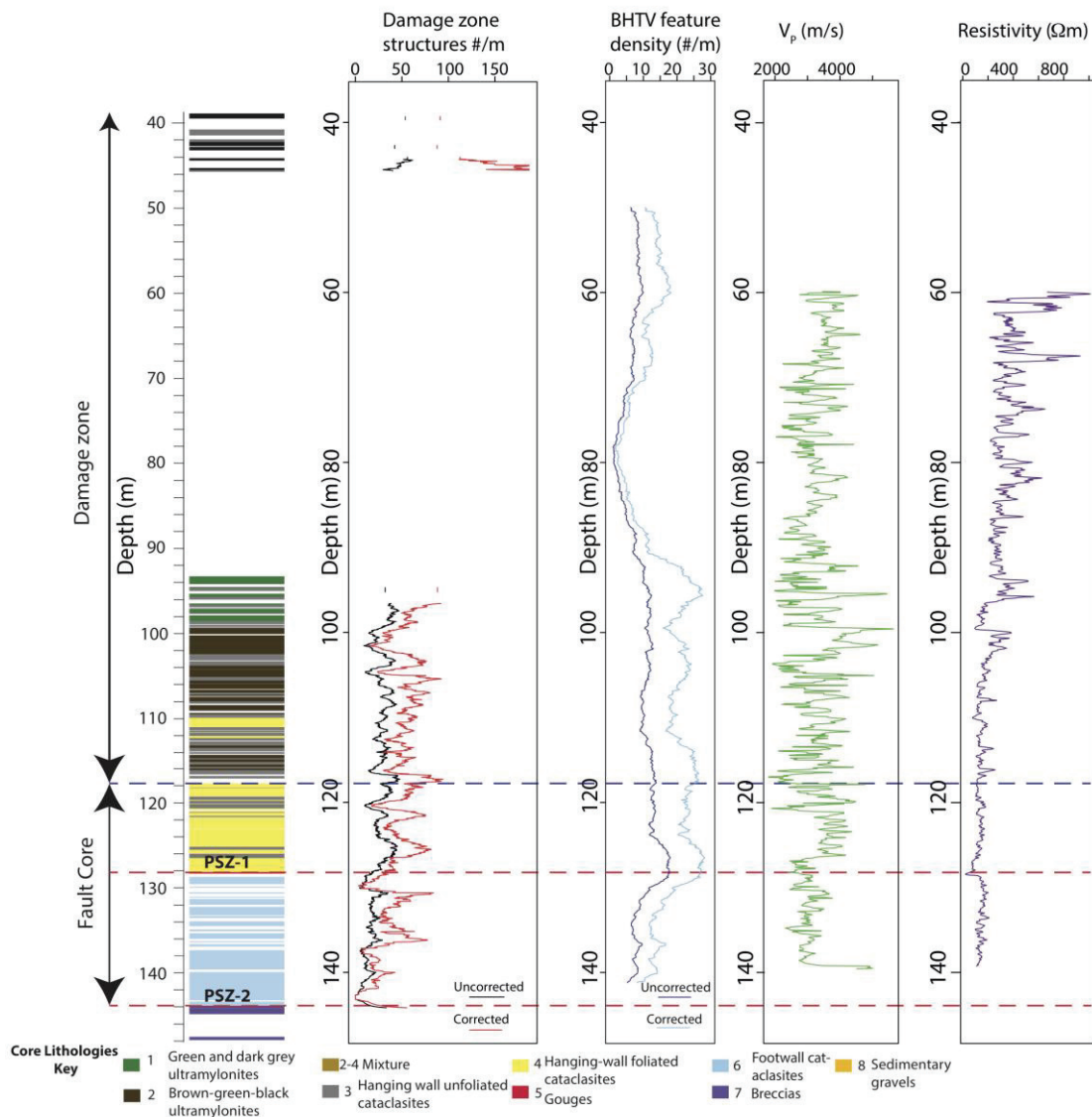
2

3 Figure 6: A comparison between borehole televiewer (BHTV) statically normalised
 4 data (two way travel time (TWTT) and amplitude) and an 'unrolled' CT image, which
 5 depicts an image of the outer surface of the drill-core, for the depth interval 107.57-
 6 108.56 m in DFDP-1B. This demonstrates that, because the resolution of the BHTV is
 7 less than that of the CT images, damage zone structures picked in the CT images may
 8 not be picked in the BHTV data.

1 Figure 7

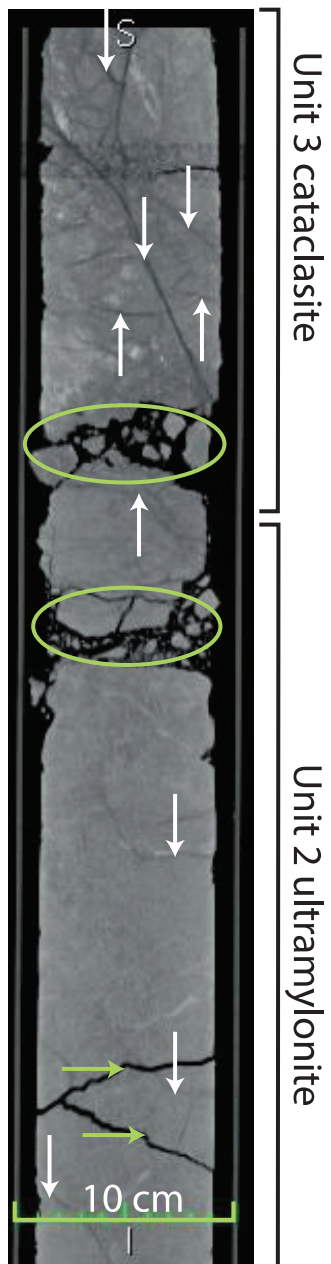


3 Figure 7: Density of damage zone structures within CT scan images of DFDP-1A
4 drill-core calculated using a moving average and weighted moving average with a 1 m
5 window size. Results are shown for cases in which a weighting has, and has not, been
6 applied to correct for orientation bias. Colours adjacent to plots reflect the DFDP-1
7 lithologies defined by Toy et al. (2015). Wireline logging data previously presented in
8 Townend et al. (2013).

1 **Figure 8**

3 Figure 8: As for Figure 7, but for the DFD-1B borehole. Additionally we show the
 4 density of damage zone structures picked in BHTV data (McNamara, 2015),
 5 calculated with a moving average at intervals of 10 cm and with a 5 m moving
 6 window to reflect the lower resolution of these data. Note that the resistivity anomaly
 7 associated with PSZ-1 is 0.2 m below that measured in the drill-core.

1 **Figure 9**

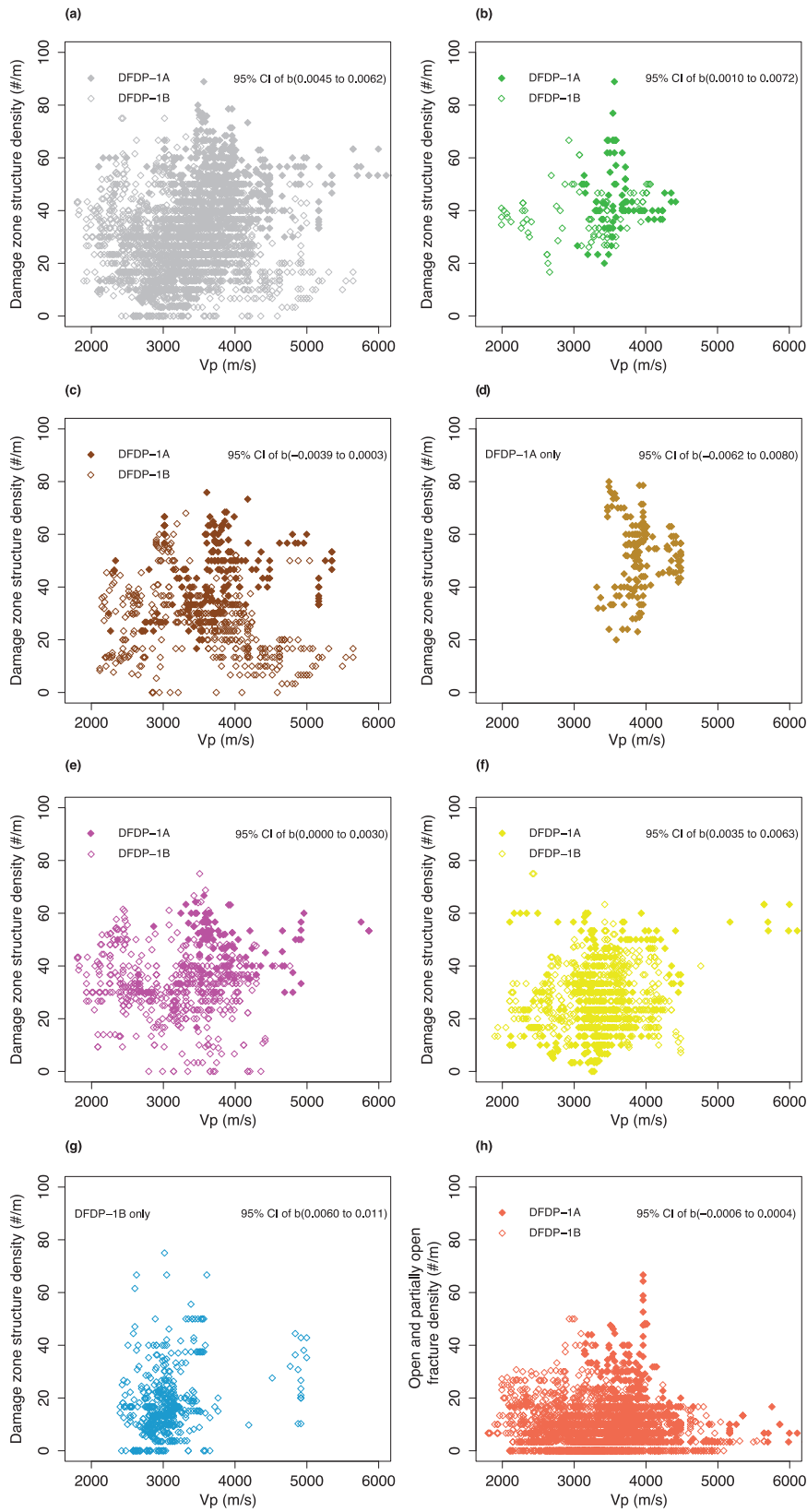


2

3 Figure 9: CT image slice of drill-core section DFD-1B 49-1, 115.50-116.05 m. This
4 section exemplifies the disparity between unit 3 cataclasite that exhibits a relatively
5 high amount of fault damage zone (denoted by vertical white arrows), compared to
6 unit 2 ultramylonites that contain relatively few damage zone structures, even though

- 7 it is only ~12 m vertical distance from PSZ-1 sampled in DFDP-1B. Horizontal green
- 8 arrows and ellipse indicate areas of induced damage in the drill-core.

1 **Figure 10**



3 Figure 10: Cross-plots of damage zone structure density, calculated using a moving
4 average with a window size of 30 cm, against P-wave velocity (V_p) obtained from
5 wireline logging (Townend et al., 2013). CI refers to the 95% confidence interval of,
6 b, the slope of the best-fit line between the damage zone structure density and V_p , to
7 four decimal places. If the CI values are close to, but both above zero, it suggests a
8 very weak positive correlation and vice versa. Values either side of zero indicate that,
9 statistically, there is no significant correlation between these parameters. (a) For all
10 data points in the DFDP-1 boreholes. (b)-(g) are selected from (a) by lithological unit:
11 (b) unit 1 ultramylonites, (c) unit 2 ultramylonites, (d) unit 2-4 mixture, (e) unit 3
12 cataclasites, (f) unit 4 cataclasites, (g) unit 6 cataclasites. (h) Cross plot calculated as
13 for all depths, but accounting for open and partially open fractures only (type v, vi and
14 vii structures, Table 1).

Figure 11

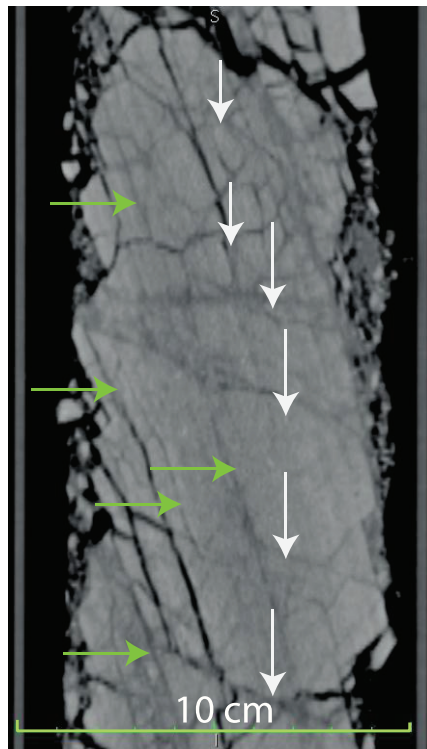


Figure 11: CT image of heavily fractured mylonite that was amongst the drill-core recovered furthest from PSZ-1 in DFDP-1B (core section 1B-25-2, depth 44.8-45.2 m). Green (horizontal) arrows identify foliation parallel filled fractures. It is unclear whether this fracture set formed as a result of seismic damage or from unloading during exhumation. White (vertical) arrows identify a non-foliation parallel set of fractures that continue to be identified in this interval.

1 **Figure 12**

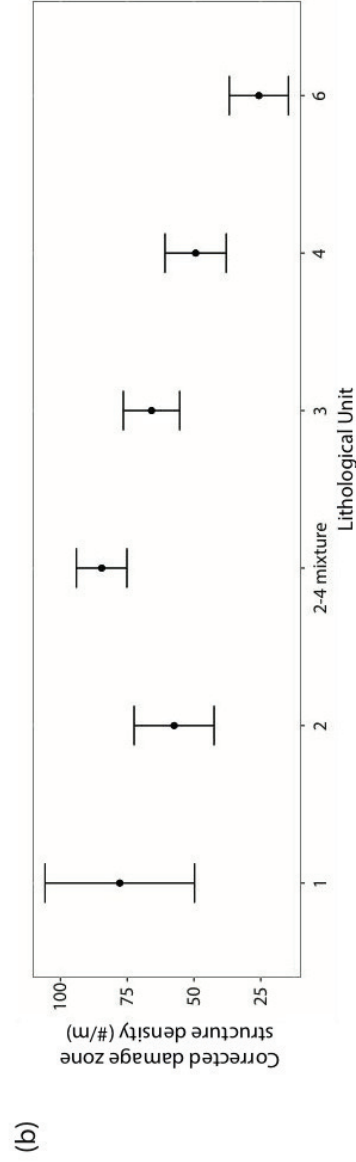
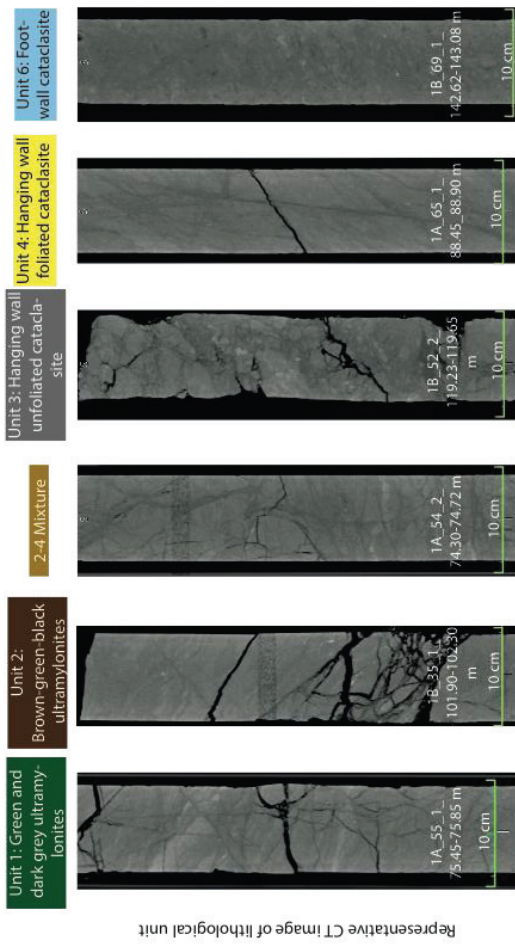
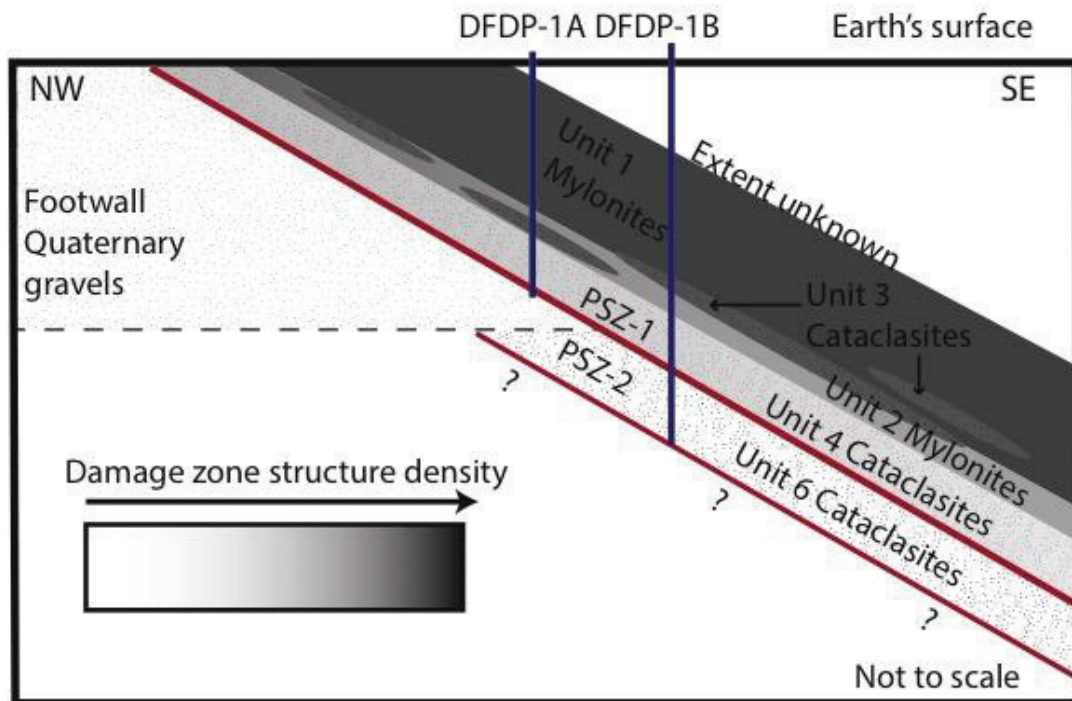


Figure 12: A representative drill-core axial parallel CT image of each DFDP-1 lithology (Toy et al., 2015) to qualitatively show how damage zone structure density varies across lithology. (b) Density of damage zone structures for each lithological unit, corrected for orientation bias. Error bars show the interquartile range of damage zone structure density calculated using a weighted moving average for each lithology.

1 **Figure 13**

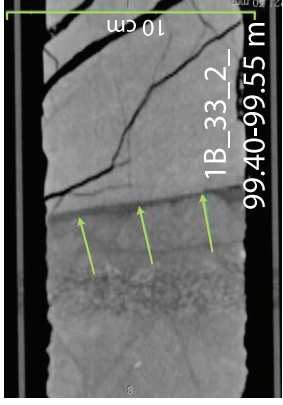
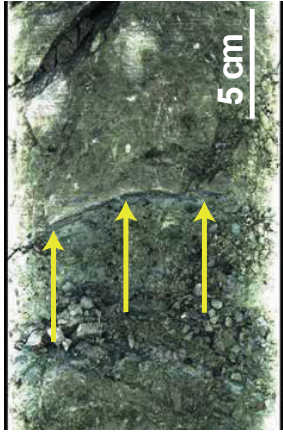




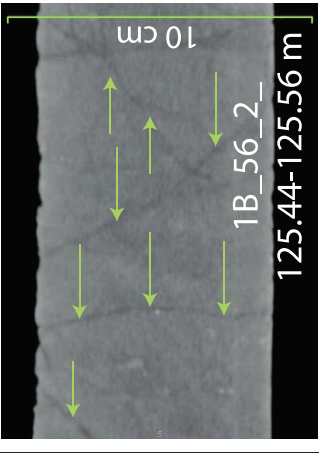

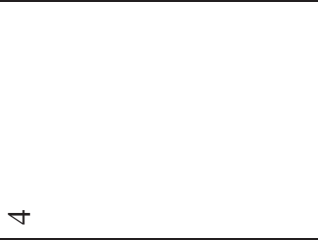

2


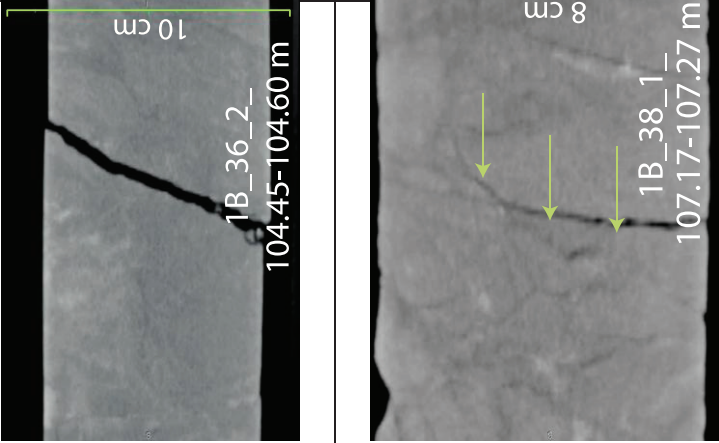
3 Figure 13: A schematic representation of the distribution of damage zone structures in
4 a cross section around the Alpine Fault, which was sampled in DFDP-1.

Table 1

Table 1

Type	CT Number Range	Aperture (mm)	Interpretation and Notes	% of damage zone structures recognised in CT images	Example in CT scan image	Equivalent image in 180° Core Scan
(i) Gouge Filled	1400-1900	>3	Small fault	10		
(ii) Cataclasite	1300-3000	>3	Cataclasite filled fault, clasts, 1-50 mm in size, of high CT (1900-3000) values, surrounded by matrix of low CT (1300-	7		

	(iii) Dark grey	1600-2200	<1-2	2000) values Clay filled fracture	50		
(iv) Grey	1900-2200	1-30	Clay filled fracture	4			

(v) Black	-1024-1200	<1-3	Open fracture	4	
(vi) Black-dark grey	-1024-2200	<1-3	Partially open fracture. Gradual change in CT number along length	21	

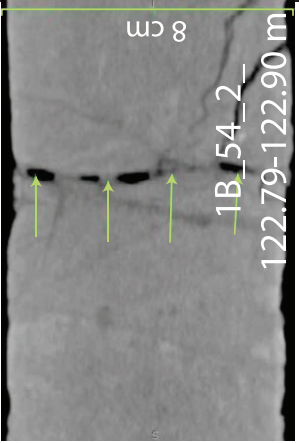

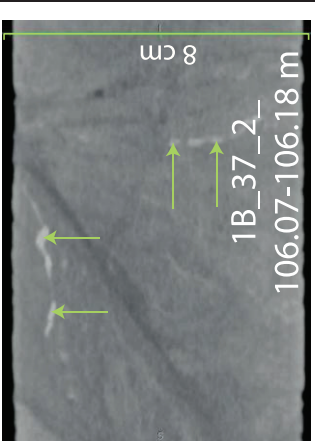

(vii) Black and dark grey	-1024-2200	<1-5	Partially open fracture. Abrupt change in CT number along length	2		
(viii) White	2300-3000	<1-5	Quartz or calcite vein	2		

Table 1: Classification scheme for describing damage zone structures observed in CT scans of DFDP-1 drill-core. Percentage of damage zone structures applies to those recognised within the alteration zone only, i.e. it excludes structures recognised in the interval of 39-45 m in the DFDP-1B borehole.